Chemical Engineering Journal 485 (2024) 149684

Contents lists available at ScienceDirect

Chemical Engineering Journal

journal homepage: www.elsevier.com/locate/cej

Methane pyrolysis in packed bed reactors: Kinetic modeling, numerical simulations, and experimental insights

Manas Mokashi [a,1], Akash Bhimrao Shirsath [a,1], Ahmet Çelik [a], Patrick Lott [a], Heinz Müller [a], Steffen Tischer [b], Lubow Maier [b], Johannes Bode [c], David Schlereth [c], Frederik Scheiff [c], Dieter Flick [c], Michael Bender [c], Kai Ehrhardt [c], Olaf Deutschmann [a,b,*]

[a] Institute for Chemical Technology and Polymer Chemistry (ITCP), Karlsruhe Institute of Technology (KIT) 76131 Karlsruhe, Germany
[b] Institute of Catalysis Research and Technology (IKFT), Karlsruhe Institute of Technology (KIT) 76344 Eggenstein-Leopoldshafen, Germany
[c] BASF SE, Group Research 67056 Ludwigshafen, Germany

ARTICLE INFO

Keywords:
High temperature kinetics
Methane pyrolysis
Hydrogen production
Fixed bed reactor
Carbon deposition
Soot formation

ABSTRACT

Pyrolysis of hydrocarbon feeds such as methane (CH_4) and natural gas emerges as a pivotal carbon dioxide-free large-scale hydrogen (H_2) production process combined with capturing the carbon as solid material. For fundamental understanding and upscaling, the complex kinetics and dynamics of this process in technically relevant reactors such as packed and moving beds still need to be explored, particularly concerning carbon formation and its impact on reactor performance. This study integrates kinetic modeling, numerical simulations, and experimental findings to comprehensively understand CH_4 pyrolysis under industrially relevant conditions and its implications for efficient H_2 production and carbon capture. The investigation covers temperatures from 1273 K to 1873 K, H_2 addition with H_2:CH_4 ratios of 0 to 4, and hot zone residence time of 1 to 7 s. Two distinct pathways lead to carbon formation: soot formation and carbon deposition. Each pathway originates from different gas-phase precursors. An elementary-step-based gas-phase reaction mechanism is coupled with a soot formation model from polycyclic aromatic hydrocarbon and a newly developed deposition model from light hydrocarbons. Numerical simulations are performed in a packed bed reactor model, incorporating a method of moments for soot formation and a model for carbon deposition. The model is evaluated against experiments and predicts the effects of operating conditions on gas-phase product distribution and carbon formation. It also estimates the change in bed-voidage over operational time. The study reveals that at the temperature 1673 K, CH_4 conversion exceeds 94 %, while both H_2 and solid carbon yields surpass 96 %. The sophisticated modeling and simulation framework presented herein thus provides an enhanced understanding of the CH_4 pyrolysis process and presents a valuable tool for optimizing this process.

1. Introduction

Hydrogen (H_2) is one of the most important raw materials in the petrochemical and chemical industry [1]. Its demand is expected to increase further as a modern carbon-free energy carrier [2–5], where circular storage solutions, i.e. using metals and metal hydrides via oxidation–reduction cycles [6–8], will play a key role. Although water electrolysis using renewable energy is at present the only carbon-free pathway to produce high purity H_2, its high investment costs and energy demands are limiting large scale application [9]. The majority of large-scale H_2 production is currently derived from fossil fuels via steam methane reforming, which accounts for almost half of this production [1]. Furthermore, dry reforming of methane (DRM) [10–12], autothermal reforming of methane (ATR) [13], and catalytic partial oxidation of methane (CPOX) [14,15] are also commercially viable alternatives based on the required syngas H_2:CO ratio [16]. Nonetheless, these processes primarily generate carbon dioxide (CO_2) as a by-product, requiring further procedures for effective carbon capture and storage [17].

Alternatively, methane (CH_4) pyrolysis presents a transitional technology towards sustainable H_2 supply, since it produces H_2 along with solid carbon without direct CO_2 emissions [2,18]. Previous studies explored catalytic CH_4 pyrolysis utilizing a wide range of catalysts,

* Corresponding author at: Bldg. 11.21, KIT-Campus South, Engesserstr. 20, 76131, Karlsruhe, Germany.
E-mail address: deutschmann@kit.edu (O. Deutschmann).
[1] Shared first authorship.

https://doi.org/10.1016/j.cej.2024.149684
Received 21 December 2023; Received in revised form 31 January 2024; Accepted 13 February 2024
Available online 19 February 2024

Nomenclature

Abbreviations

CVD	Chemical vapor deposition
HACA	Hydrogen Abstraction Carbon Addition
PAH	Polycyclic aromatic hydrocarbons
PSD	Particle size distribution
SCF	Stokes–Cunningham factor

List of symbols Latin symbols

A	Pre-exponential factor $m^3\ mol^{-1}\ s^{-1}$ or $m\ s^{-1}$
a_v	Area to volume ratio m^{-1}
$c^{deposition}$	Concentration of deposition species $mol\ m^{-2}$
c^{gas}	Concentration of gas-phase species $mol\ m^{-3}$
$c^{surface}$	Concentration of (non-deposition) surface species $mol\ m^{-2}$
d_c	Collector unit diameter m
d_d	Effective diameter of dimer m
d_p	Bed particle diameter m
d_{pore}	Mean pore diameter m
$d_{p,\ soot}$	Soot particle diameter m
$D_{soot,i}$	Soot particle diffusion coefficient $m^2\ s^{-1}$
E	Soot filtration efficiency -
E_A	Activation energy $kJ\ mol^{-1}$
E_d	Enhancement factor -
f	friction factor -
$\dot{I}$	Dimensionless nucleation rate -
K	Kuwabara's hydrodynamic factor -
Kn	Knudsen number -
k	Rate constant $m^3\ s^{-1}$ or $m\ s^{-1}$
k_B	Boltzmann constant $m^2\ kg\ s^{-2}\ K^{-1}$
M	Molar mass $kg\ mol^{-1}$
M_d	Reduced mass of the dimer kg
M_0	zeroth moment m^{-3}
M_1	First moment $m^3\ m^{-3}$
M_2	Second moment $m^3\ m^3\ m^{-3}$
m_m	Initial monomer mass kg
N_A	Avogadro number mol^{-1}
$\dot{N}$	Dimensionless particle number concentration -
n_m^*	Dimensionless monomer concentration -
p	Pressure Pa
Pe	Peclet number -
$\dot{s}$	Rate of surface reaction $mol\ m^{-2}\ s^{-1}$
S_g	Set of gas-phase species -
St	Stokes number -
t	Time s
T	Gas phase temperature K
u	Superficial velocity of gas $m\ s^{-1}$
u_{pore}	Interstitial or pore velocity $m\ s^{-1}$
$\dot{V}_1$	Dimensionless particle volume concentration -
$\dot{V}_2$	Dimensionless second aerosol volume moment -
v_g	geometric mean volume -
$\dot{W}$	Dimensionless soot surface growth rate -
Y	mass faction of species -
z	Reactor axial coordinate m

Greek symbols

α	Fraction of surface site available -
ε_{bed}	Bed-voidage -
η	Single bed particle efficiency -
$\eta_{Diffusion}$	Single sphere Brownian efficiency -
$\eta_{Inertial}$	Single sphere inertial efficiency -
$\eta_{Interception}$	Single sphere interception efficiency -
Θ	Dimensionless residence time -
λ	Gas mean free path m
μ	Dynamic gas viscosity $kg\ m^{-1}\ s^{-1}$
ξandζ	Dimensionless coagulation coefficients -
ρ	Gas phase density $kg\ m^{-3}$
ρ_{soot}	Soot density $kg\ m^{-3}$
σ_g	geometric standard deviation -
$\chi_{C_{soot}H}$	sites per unit surface area of the particles site m^{-2}
$\dot{\omega}$	Rate of gas phase reaction $mol\ m^{-3}\ s^{-1}$

including metal catalysts [4,19,20], carbon-based materials [21–23], and unfunctionalized carriers [23,24]. However, it was observed that carbon deposition during operation resulted in relatively rapid catalyst deactivation [20,25]. Furthermore, alternative processes for CH_4 pyrolysis such as the liquid metal bubble column reactor [26] and plasma pyrolysis [27–29] have been reported. However, these technologies remain in the preliminary stages of development.

In contrast, thermal methane pyrolysis has been studied and reported as a viable alternative to the above mentioned processes [30,31] that in principle allows large-scale H_2 production via CH_4 pyrolysis, for instance as demonstrated by a demo plant that was put into operation by BASF SE in 2021 [32]. Additionally, studies have reported that the presence of solid carbon accelerates the carbon deposition [30,33,34]. Two different pathways resulting in the formation of solid carbon during pyrolysis of light hydrocarbons can be found in the literature: soot formation from polycyclic aromatic hydrocarbons (PAHs) in an empty tube reactor or flames [35–40] and direct deposition through light hydrocarbons on reactor wall or packing material [33,34,41–47]. Earlier studies on the formation of carbon in the form of soot found that the particle number concentration of soot formed during pyrolysis was directly related to operating conditions, PAH concentrations and temperature [48,49]. A series of gas-phase reactions lead to soot nucleation followed by coagulation, sintering, surface growth and condensation [37]. Many approaches were proposed to approximate the general equations of dynamics, including the monodisperse model [40,50,51], the method of moments [52–54], the sectional method [55–57], the stochastic model [58] and the Galerkin model [59]. On the other hand, direct carbon deposition from CH_4, ethylene (C_2H_4), acetylene (C_2H_2), butadiene (C_4H_6), propylene (C_3H_6) and benzene (C_6H_6) was also found to be dependent on temperature, hydrocarbon inlet concentrations, pressure and the available surface area for deposition [41–46]. Furthermore, Becker et al. [60] reported that the presence of H_2 inhibits the deposition reactions. On the basis of work by Becker et al. [60], Li and Deutschmann [47] elaborated on chemical vapor infiltration (CVI) from CH_4 under sub-atmospheric pressure and coupled a deposition mechanism with reduced gas-phase kinetics while considering H_2 inhibition.

In spite of these promising studies, none of them investigated CH_4 pyrolysis in a packed bed reactor for the formation of H_2 and carbon. Hence, our present study employs a combined approach of lab-scale packed bed reactor experiments and numerical simulations using detailed kinetics to investigate the CH_4 pyrolysis process under industrially relevant conditions. Covering a wide range of operating conditions, namely temperatures above 1273 K, varying H_2:CH_4 ratios (1, 2, and 4), and residence times (1, 3, 5, and 7 s), the behavior of the system is comprehensively examined. The study incorporates an improved carbon deposition kinetic model derived from light hydrocarbons, as well as a soot formation model. In addition, the developed model incorporates the concept of the filtration mechanism to evaluate and account for the trapping of soot particles within the packed bed material. Furthermore, the detailed gas-phase mechanism proposed by Appel et al. [35] is coupled with the deposition and soot model. By integrating

these aspects, the model is evaluated with the aim to provide a more detailed understanding of the carbon deposition and soot formation in CH_4 pyrolysis. This comprehensive approach enables the analysis of interaction between gas-phase reactions, deposition kinetics, and soot particle growth, expanding our knowledge of the overall system behavior and allowing for an improved design of CH_4 pyrolysis processes for large-scale H_2 production.

2. Experimental

Experiments were performed in a tubular flow reactor designed for kinetic studies at high temperature (up to 2073 K) and high pressure (up to 10 bar) as shown in the schematic in Fig. 1. The flow diagram of the experimental setup is provided in Fig. S1. More details about the setup are described in a previous publication by Angeli et al. [61]. The α-Al_2O_3 tubular reactor of 0.02 m inner diameter and 1.0 m length was placed in a stainless-steel vessel equipped with heating elements and insulation, which results in an isothermal zone of 0.4 m. The packed bed (length of 0.12 m) consisting of acetylene coke particles (approx. 0.002 m diameter) was kept in a graphite foil container, which is open at the top and has holes at the bottom to allow the effluent gas stream exiting the packed bed. After placing the container at the beginning of isothermal zone, the reaction gas mixture was fed into the reactor via mass flow controllers while controlling the operating conditions by a LabView-based software. The product gas stream was continuously analyzed with an HPR-20 mass spectrometer (Hiden Analytical), particularly quantifying H_2, CH_4, C_2H_2, C_2H_4, C_2H_6 and C_6H_6. The operating conditions chosen for the present study are summarized in Table 1.

3. Modeling approach and numerical simulation

In order to fully understand the CH_4 pyrolysis process, it is essential to develop a comprehensive model that considers the various phenomena occurring within the laboratory reactor as depicted in Fig. 2. This model should include elements such as gas-phase reactions, solid carbon deposition, soot formation and growth, and its interactions with the packed bed. The subsequent section provides details on the kinetic models as well as strategies for their effective coupling.

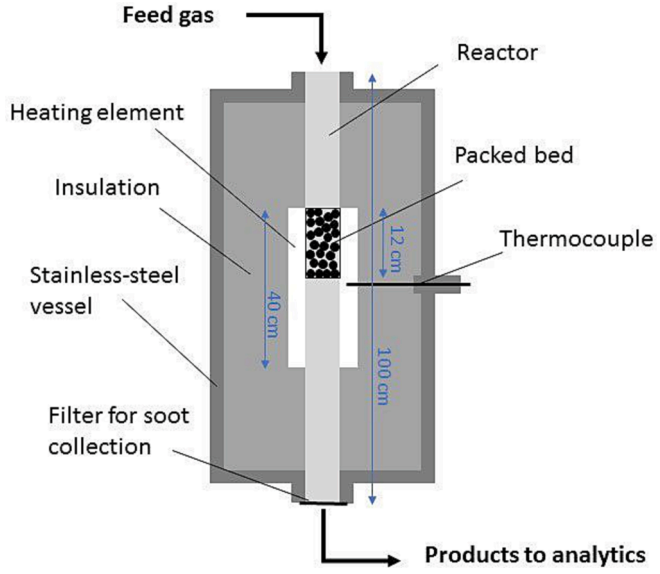

Fig. 1. Experimental setup.

Table 1
Experimental conditions during reactor operation.

Process parameter	Variation range
Temperature	1273 – 1373 – 1473 – 1573 – 1673 K
H_2:CH_4 molar feed ratio	1 – 2 – 4
Residence time	5 s
Pressure	1 bar

3.1. Kinetic modeling

3.1.1. Gas-phase reactions

Since the CH_4 pyrolysis reaction starts with gas-phase species, a reliable gas-phase elementary-step based mechanism is critical. For the present work, a detailed gas-phase mechanism by Appel et al. [35] that was originally developed for describing the combustion of C_2 hydrocarbons, hereinafter referred to as ABF2000, was employed. To adapt it to pyrolysis conditions, all oxygen-related species and reactions were removed, leading to a shortened mechanism comprising 247 reactions and 76 species. The choice of ABF2000 was driven by the presence of polycyclic aromatic hydrocarbons (PAHs) formation in this mechanism, which are considered to be a crucial factor for coupling the soot formation model to gas-phase reactions. When PAHs species collide with each other (pyrene in case of ABF2000), dimers are assumed to form that result in the formation of soot clusters [36,62]. In particular, pyrene helps to overcome the thermodynamic barrier between two and three rings, and the dimer is responsible for nucleating soot. To validate this assumption, Schuetz and Frenklach [62] studied the formation of pyrene dimers by using molecular dynamics simulations, which showed that at a temperature of 1600 K, 15 % of the collisions resulted in stable dimers with a lifetime exceeding 10 ps. These findings suggest that pyrene dimers may act as soot nuclei under certain conditions. The nucleation rate is assumed to be the collision rate of two $C_{16}H_{10}$ (pyrene) molecules in the free-molecular region, with a van der Waals enhancement factor of 2.2 being taken into account [63–66]. To incorporate this information in the soot model, the chemical source term utilized is the net production rate of the dimers. The chemical source term for the soot model is determined by integrating the pyrene dimer formation reaction and rate constant into the ABF2000 mechanism shown in Eqs. (1) and (2), respectively [67,68],

$$C_{16}H_{10} + C_{16}H_{10} \rightarrow \text{Dimer} \tag{1}$$

$$k = E_d d_d^2 \sqrt{\frac{8\pi k_B T}{M_d}} \tag{2}$$

where, E_d is enhancement factor, d_d is effective dimer diameter, k_B is Boltzmann constant, T the temperature, and M_d is reduced mass of the dimer.

3.1.2. Soot surface growth kinetics

Soot surface growth is a crucial aspect of the CH_4 pyrolysis process, and several mechanisms have been proposed to explain the growth dynamics [35,36,56,69]. One widely accepted model is the HACA (H-abstraction C_2H_2-addition) surface growth mechanism suggested by Appel et al. [35]. The HACA mechanism has been extensively studied and validated through experimental and theoretical studies, providing a detailed understanding of the surface kinetics of soot growth [35–37,58]. For the current study, the HACA surface growth mechanism was modified by removing all oxygen-related reactions, resulting in the modified growth rate depicted in Eq. (3). The rate constants for this modified growth rate are presented in Arrhenius format in Table 2. For the present study, both the surface site density and the fraction of surface sites available for the reaction are obtained from the literature [36].

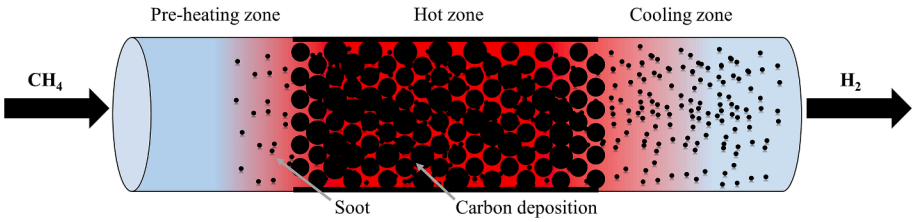

Fig. 2. Methane pyrolysis in a packed bed reactor: gas-phase reactions, soot formation and carbon deposition.

Table 2
Kinetic mechanism for soot surface growth [35,36].

Soot surface growth kinetic data in Arrhenius format				
Rate constant	Reaction	A(m^3 mol^{-1} s^{-1})	n	E_A(kJ mol^{-1})
k_1	C_{soot} −H + H→$C_{soot\cdot}$ + H_2	4.17E + 7	–	54.40
k_{-1}	$C_{soot\cdot}$ + H_2→C_{soot} −H + H	3.9E + 6	–	46.02
k_2	$C_{soot\cdot}$ + H→C_{soot} −H	2.0E + 7	–	–
k_3	$C_{soot\cdot}$ + C_2H_2→C_{soot} −H + H	80.0	1.56	15.90

$$k = 2\frac{\alpha\chi_{C_{soot}H}k_3[C_2H_2]k_1[H]}{k_{-1}[H_2] + k_2[H] + k_3[C_2H_2]} \tag{3}$$

where, α is fraction of surface site available, and $\chi_{C_{soot}H}$ is sites per unit surface area of the particles.

3.1.3. Carbon deposition and hydrogen inhibition kinetics

The chemical vapor deposition (CVD) from light hydrocarbons is considered to be a complex surface reaction where solid carbon is deposited from gaseous light hydrocarbons [33,47,60,70,71]. As mentioned above, gas-phase reactions are described using the ABF2000 mechanism. In a next step, the heterogeneous surface reactions were then coupled to the deposition precursors from ABF2000. The reaction mechanism of CVD from gas-phase hydrocarbon was first proposed by Becker et al. [60] and later employed by Li and Deutschmann [47] for describing chemical vapor infiltration (CVI). CH_4 pyrolysis in the current study takes place in a flow reactor and at atmospheric pressure. Therefore, the work by Li and Deutschmann [47] was extended by selecting additional deposition precursors as illustrated in Fig. 3 based on a gas-phase mechanistic study on CH_4 pyrolysis using the ABF2000 mechanism [72]. While activation energy values were taken from the work by Tesner [70], pre-exponential factors were fitted to the packed bed experiments, which further improved the H_2 inhibition functions. The resulting updated kinetic parameters used in the present study are summarized in Table 3.

3.2. Packed bed reactor model

In this study, a one-dimensional packed bed reactor model was employed to simulate CH_4 pyrolysis experiments conducted in a laboratory reactor. The model simulates the chemically reacting flow of a gas mixture in axial direction under steady-state conditions, and solves the continuity equation, species conservation equation, pressure drop, and equation of state using a differential–algebraic solver (LIMEX)[73,74].

Table 3
Kinetic parameters for deposition reactions with H_2 inhibition function.

Deposition reaction kinetic data in Arrhenius format			
Species	A(m s^{-1})	E_A(kJ mol^{-1})	H_2 inhibition function
CH_4	4.00E + 12	446	$2.094/\left(2.094+\frac{[H_2]}{[CH_4]}\right)$
C_2H_6	1.00E + 13	268	$1.594/\left(1.594+\frac{[H_2]}{[C_2H_6]}\right)$
C_2H_4	7.25E + 03	155	$1.594/\left(1.594+\frac{[H_2]}{[C_2H_4]}\right)$
C_2H_2	2.03E + 02	126	$4.497/\left(4.497+\frac{[H_2]}{[C_2H_2]}\right)$
C_4H_6	7.25E + 02	142	$6.042/\left(6.042+\frac{[H_2]}{[C_4H_6]}\right)$
C_6H_6	2.35E + 06	217	$0.519/\left(0.519+\frac{[H_2]}{[C_6H_6]}\right)$

The equation of continuity, represented by Eq. (4), is used to calculate the mass flux in a system.

$$\frac{d(\rho u)}{dz} = a_v\sum_{i\in S_g} M_i\dot{s}_i \tag{4}$$

where, ρ is gas phase density, u is superficial velocity of gas, z is reactor axial coordinate, a_v is surface area to volume ratio, M_i is molar mass of species i, $\dot{s}$ is rate of surface reaction, and S_g is set of gas-phase species.

Along with Eq. (4), the species conservation Eq. (5) is solved.

$$\rho u\frac{dY_i}{dz} = M_i\left(a_v\dot{s}_i + \dot{\omega}_i\varepsilon_{bed}\right) - Y_i a_v\sum_{i\in S_g} M_i\dot{s}_i \tag{5}$$

where, Y_i is mass faction of species i, $\dot{\omega}_i$ is rate of formation of gas-phase species i, and ε_{bed} is packed bed-voidage.

Furthermore, the pressure drop in the packed bed reactor is calculated based on Eq. (6)

$$\frac{dp}{dz} = f\frac{\rho u^2}{d_p} \tag{6}$$

where, p is pressure, f is friction factor and d_p is bed particle diameter.

The friction factor f is calculated based on the Ergun Equation [75].

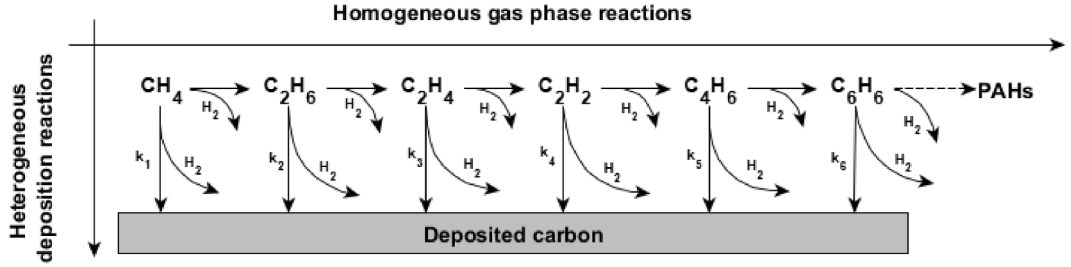

Fig. 3. Extended deposition model from various gas-phase precursors.

Furthermore, in this study, the energy balance equation was not explicitly solved. Instead, the experimentally measured temperature profiles within the reactor were used as an input parameter. By directly incorporating the measured temperature profile, the model can focus on simulating the chemical reactions and species transport within the system while maintaining consistency with the experimental conditions.

The DETCHEM software package [74,76–80] was used to perform packed bed reactor ($DETCHEM^{PBR}$) simulations where a transient wrapper ($DETCHEM^{PBR\_transient}$) calculates carbon deposition as a function of operation time. This simulation assumes that the time scale for deposition reactions is much longer than the residence time of the gas phase. The transient wrapper calls the $DETCHEM^{PBR}$ simulation iteratively at each time step, performing a quasi-steady-state simulation to calculate the concentration profiles of the gas-phase species, while keeping the concentrations of the deposition species fixed. However, coverage varies depending on the location within the reactor. The locally resolved gas-phase concentrations are then transferred back to the transient wrapper for a time integration step for the transient species Eq. (7). The simulation process is completed by repeating the steady-state packed bed reactor simulation with updated inlet conditions and the newly updated state of the surface.

$$\frac{dc_i^{\text{deposition}}}{dt} = \dot{s}_i\left(c^{\text{gas}}, c^{\text{surface}}, c^{\text{deposition}}\right) \tag{7}$$

where, $c^{\text{deposition}}$ is concentration of deposited species, c^{gas} is gas-phase concentration, and c^{surface} is concentration of non-deposited surface species.

3.3. Method of moment model

The modeling of soot formation plays a significant role in comprehending and optimizing the CH_4 pyrolysis process. The method of moments (MOM) is a widely used approach to model the time evolution of the size and number density of soot particles through a set of moment equations [63,69,81–86].

These equations consider the key phenomena of nucleation, growth, and coagulation that govern the behavior of soot particles. Based on the assumption that soot particles are spheres and homogeneous, the MOM model can provide insight into how temperature, pressure, and reactant concentration affect nucleation, growth, and coagulation.

For the present work, instead of solving for the entire particle size distribution (PSD), we focus on the first three moments (M_0, M_1 and M_2), hereby capturing the most important aspects of the process. The governing equations for the lognormal moment model were written in a dimensionless form in terms of moment change rates. The zeroth moment M_0 represents the total particle number concentration N and is affected by nucleation and coagulation, as shown in Eq. (8).

$$\frac{dN^{'}}{d\Theta} = I^{'} - \xi N^{'2} \tag{8}$$

where, $N^{'}$ is dimensionless particle number concentration, Θ is dimensionless residence time, $I^{'}$ is dimensionless nucleation rate, and ξ is dimensionless coagulation coefficient.

For the present study, the dimensionless coagulation coefficient ξ are the harmonic average of coefficients in the free molecular ξ_{FM} and continuum regimes ξ_C (see SI, Equations (S1)–(S5)). The first moment M_1 represents the particle volume concentration V_1 and is affected by both nucleation and surface growth, as shown in Eq. (9).

$$\frac{dV_1^{'}}{d\Theta} = I^{'} n_m^{*} + W^{'} \tag{9}$$

where, $V_1^{'}$ is dimensionless particle volume concentration, n_m^{*} is dimensionless monomer concentration, and $W^{'}$ is dimensionless soot surface growth rate.

The second moment M_2 represents the particle volume V_2 and is affected by nucleation, surface growth, and coagulation, as shown in Eq. (10).

$$\frac{dV_2^{'}}{d\Theta} = I^{'} n_m^{*2} + 2\zeta V_1^{'2} + W^{'} \tag{10}$$

where, $V_2^{'}$ is dimensionless second aerosol volume moment, and ζ is dimensionless coagulation coefficient, calculated as harmonic average of coefficients in the free molecular ζ_{FM} and continuum regimes ζ_C (see SI, Equations (S6)–(S9)).

Assuming spherical particles, the mean particle diameter $d_{p,soot}$ can be calculated using Eq. (11).

$$d_{p,soot} = \left(\frac{6 m_m M_1}{\pi \rho_{soot} N_A M_0}\right) \tag{11}$$

where, $d_{p,soot}$ is soot particle diameter, m_m is initial monomer mass, M_1 is first moment, ρ_{soot} is soot density, N_A is Avogadro number, and M_0 is zeroth moment.

The PSD is assumed to follow a lognormal distribution, which allows the geometric mean volume (v_g, Eq. (12)) and geometric standard deviation (σ_g, Eq. (13)) to be expressed in terms of the first three moments (M_0, M_1 and M_2) of the PSD.

$$v_g = \frac{M_1^2}{M_0^{3/2} M_2^{1/2}} \tag{12}$$

$$\ln^2 \sigma_g = \frac{1}{9} \ln\left(\frac{M_0 M_2}{M_1^2}\right) \tag{13}$$

where, v_g is geometric mean volume, and σ_g is geometric standard deviation.

3.4. Soot filtration model

The deposition of soot on the carbon particles of the packed bed is a critical aspect that significantly impacts the system's overall performance. To address this phenomenon, the modeling approach has been expanded to incorporate the concept of a filtration mechanism. The presented method, illustrated in Fig. 4, effectively captures the behavior

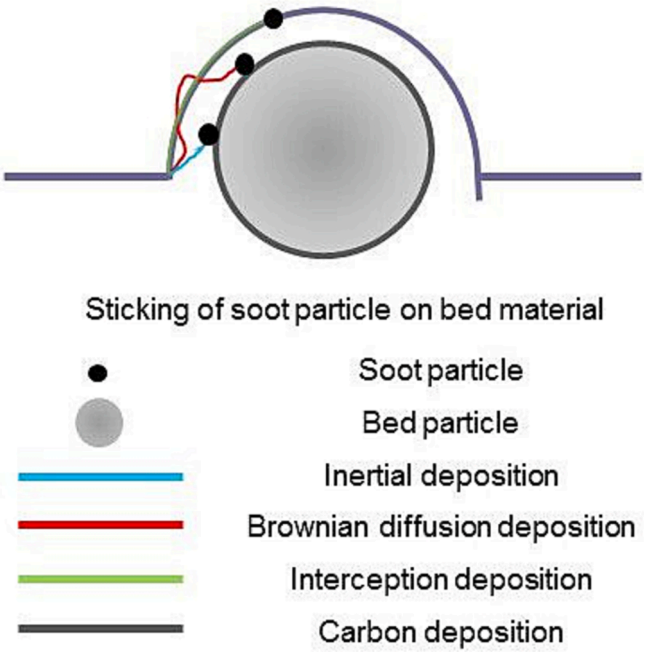

Fig. 4. Soot deposition mechanisms on packed bed particle.

of soot deposition in a packed bed by considering various mechanisms, including Brownian diffusion, interception, and inertia.

The efficiency of soot capture in 0a packed bed is determined by breaking the bed down into several zones and by introduction of a zone efficiency E_i (Eq. (14)), which is based on the local porosity and pore size at any given time [87,88].

$$E_i = 1 - \exp\left(\frac{-3\eta_i(1-\varepsilon_{bed})dz_i}{2\varepsilon_{bed}d_c}\right) \tag{14}$$

Herein, d_c is the diameter of the spherical collectors constituting a packed bed and calculated as shown in Eq. (15). Furthermore, total mass m_d and density ρ_d takes both, carbon accumulated due to deposition reactions and entrapped soot particles.

$$d_c = \left(d_{c,0}^3 + \left(\frac{6m_d}{\pi\rho_d}\right)\right)^{\frac{1}{3}} \tag{15}$$

The initial collector diameter $d_{c,0}$ is determined from the clean packed bed's voidage $\varepsilon_{bed,0}$ and pore diameter $d_{pore,0}$.

$$d_{c,0} = \frac{3(1-\varepsilon_{bed,0})^2}{2\varepsilon_{bed,0}}d_{pore,0} \tag{16}$$

The E_i is calculated using a single bed particle efficiency η_i according to Eq. (17). η_i is calculated using a mass balance of particles and the pore velocity as a characteristic velocity for the particles [89].

$$\eta_i = \left(\eta_{Diffusion,i} + \eta_{Interception,i} + \eta_{Inertial,i}\right) - \left(\eta_{Diffusion,i}\eta_{Interception,i} + \eta_{Interception,i}\eta_{Inertial,i} + \eta_{Diffusion,i}\eta_{Inertial,i}\right) + \eta_{Diffusion,i}\eta_{Interception,i}\eta_{Inertial,i} \tag{17}$$

where, $\eta_{Diffusion}$ is single sphere Brownian efficiency, $\eta_{Interception}$ is single sphere interception efficiency, and $\eta_{Inertial}$ is single sphere inertial efficiency.

3.4.1. Inertial deposition

Inertial deposition occurs when particles in a fluid flow are unable to change their trajectory as the flow approaches the surface of a bed particle. This leads to larger particles being deposited on the bed particle through impaction. The efficiency of inertial deposition for a single soot particle can be described by the Stokes number in Eq. (18) and calculated using Eqs. (19)–(21) [90,91].

$$\eta_{Inertial,i} = \frac{St_i^2}{(St_i + 0.25)^2} \tag{18}$$

$$St_i = \frac{SCF\rho_{soot}u_{pore,i}d_{p,soot,i}^2}{9\mu d_c} \tag{19}$$

$$SCF = 1 + Kn\left(1.257 + 0.4\ e^{\frac{1.1}{Kn}}\right) \tag{20}$$

$$Kn = \frac{2\lambda}{d_{pore}} \tag{21}$$

where, St is Stokes number, SCF is Stokes–Cunningham factor, u_{pore} is interstitial or pore velocity, μ is dynamic gas viscosity, d_c is collector unit diameter, and Kn is Knudsen number.

3.4.2. Brownian diffusion deposition

At low flow velocities, Brownian diffusion [87,92] is the main mechanism for depositing small particles on a surface. As the size of soot particles decreases, their motion is increasingly affected by Brownian motion, causing them to diffuse away from the streamlines and be deposited on a carbon particle of the packed bed. By accounting for the Peclet number and Kuwabara's hydrodynamic factor (K), the efficiency of Brownian diffusion deposition for a single sphere can be calculated using the provided Eqs. (22)–(25).

$$\eta_{Diffusion,i} = 3.5\left(\frac{\varepsilon_{bed}}{K}\right)^{\frac{1}{3}}Pe_{bed,i}^{-\frac{2}{3}} \tag{22}$$

$$Pe_{bed,i} = \frac{u_{pore,i}d_{c,0}}{D_{soot,i}} \tag{23}$$

$$D_{soot,i} = \frac{Tk_B SCF}{3\pi\mu d_{p,soot,i}} \tag{24}$$

$$K = 2 - \varepsilon_{bed} - \frac{9}{5}(1-\varepsilon_{bed})^{\frac{1}{3}} - \frac{1}{5}(1-\varepsilon_{bed})^2 \tag{25}$$

where, K is Kuwabara's hydrodynamic factor, Pe is Peclet number, and k_B is Boltzmann constant.

3.4.3. Interception deposition

The interception mechanism is a way for bed particles to collect particles whose diameter is larger and whose trajectory does not deviate from the streamline [87,93]. This occurs when the streamline brings the particle close enough to the surface of the bed particle for it to get stuck. The efficiency of this mechanism depends on the relative size of the soot particle and the bed particle. The efficiency of interception deposition for a bed particle in a packed bed can be calculated using the Eq. (26).

$$\eta_{Interception,i} = \frac{3\left(\frac{d_{p,soot,i}}{d_c}\right)^2}{2\left(1 + \left(\frac{d_{p,soot,i}}{d_c}\right)^{\frac{3-2\varepsilon_{bed}}{3\varepsilon_{bed}}}\right)}\frac{\varepsilon_{bed}}{K} \tag{26}$$

The efficiency of soot capture in each zone is calculated by evaluating the impact of soot particle buildup on the microstructure of the packed bed.

4. Results and discussion

4.1. Impact of temperature and hydrogen dilution

Based on an experimental assessment of the reaction conditions [30] as well as the analysis of the modified ABF2000 gas-phase mechanism, temperature and H_2:CH_4 molar feed ratio emerged as critical process parameters during CH_4 pyrolysis. This section examines the impact of these parameters after coupling the gas-phase ABF2000 model with the deposition and soot models, hereby covering both homogeneous and heterogeneous reactions.

4.1.1. Gas-phase species

In a first step, an end-of-pipe analysis was performed to compare experimental results with simulations. Fig. 5 illustrates end-of-pipe CH_4 conversions, H_2 yields and by-product mole fractions for both experiments and simulations. Fig. 5 (a) and (b) shows the gas-phase product distribution for major and minor species at different temperatures and H_2:CH_4 molar feed ratio of 1. Under these conditions, the good agreement is obtained for major species, whereas minor species shows visible deviations from experimental data. Additionally, simulations were conducted to assess the current coupled model (gas-phase, carbon deposition, and soot formation) and the gas-phase mechanism (ABF2000) against experimental data. The evaluation was conducted using the root mean square error (RMSE) method, and the results can be found in Table S1. A RMSE of above 10 % was found major species when using the ABF2000 mechanism, whereas the current model results in an average RMSE of less than 5 %. In comparison to ABF2000, the current model performed better in terms of alignment with the experimental data. Furthermore, Fig. 5(c), CH_4 conversion in the experiments for a H_2:CH_4 molar feed ratio of 2 and a residence time of 5 s begins at 1273 K and rises rapidly to 84 % at 1573 K before essentially reaching full

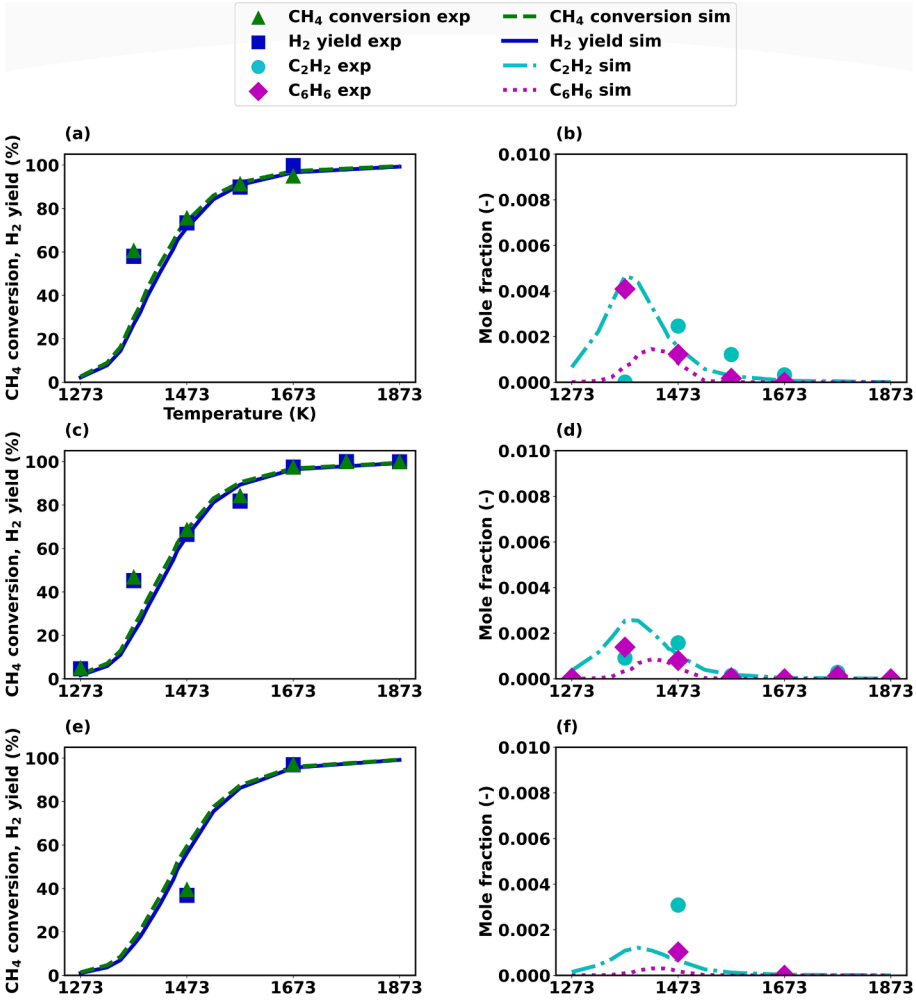

Fig. 5. End-of-pipe analysis vs. temperature at $\tau = 5$ s, $p = 1$ bar: CH_4 conversion and H_2 yield vs. temperature for (a) H_2:CH_4 ratio of 1; (c) ratio of 2, and (e) ratio of 4; and by-product mole fraction vs. temperature for (b) H_2:CH_4 ratio of 1; (d) ratio of 2, and (f) ratio of 4.

conversion at 1873 K. H_2 yield correlates closely with CH_4 conversion and reaches 100 % at 1873 K. Throughout all conditions evaluated, the combined yield of all the by-products remains below 5 %. Nevertheless, the mole fractions of the main by-products at these conditions, namely C_2H_2 and C_6H_6, are shown in Fig. 5(d). Both the by-products reach a peak value at intermediate temperatures, however, do not survive at temperatures above 1673 K. At 1473 K and a H_2:CH_4 feed ratio of 1, a CH_4 conversion of 76 % is obtained in the experiments, which reduces to 40 % when the ratio is increased to 4 (Fig. 5(a) and (e)). If a higher temperature of 1673 K is chosen, the effect of the H_2:CH_4 ratio on CH_4 conversion and H_2 yield becomes negligible and the CH_4 pyrolysis is primarily governed by the reactor temperature. Simulations and end-of-pipe measurements are in good agreement with regard to CH_4 conversion and H_2 yield as well as for the by-products above 1473 K for which, however, there is a noticeable discrepancy between 1273 and 1473 K (Fig. 5(b), (d), (f)).

As demonstrated in Fig. 5 with the end-of-pipe measurements, examining the axial profiles is equally crucial for a comprehensive understanding of CH_4 pyrolysis. The simulated axial profiles of H_2 formation for different temperatures and H_2:CH_4 molar feed ratios are shown in Fig. 6 and compared with end-of-pipe experimental measurements. For temperatures higher than 1573 K, the H_2 formation starts already in the pre-heating zone in front of the packed bed. However, a further rapid increase in H_2 formation can be seen at the beginning of the bed for all temperatures and H_2:CH_4 feed ratios. Apart from the case of a H_2:CH_4 feed ratio of 4 and a temperature of 1473 K, where the simulation tends to over predict the H_2 formation as depicted in Fig. 6 (c), the simulations conducted after coupling the ABF2000 gas phase mechanism with the deposition and soot model predict the experimental data with high accuracy.

For the conditions investigated in this study, the H_2 yield is always comparably high, while the formation of gaseous by-products occurs in minimal quantities. This is seen in the end-of-pipe experimental results in Fig. 7 and Fig. 8 for C_2H_2 and C_6H_6, respectively. In line with previous studies [30,31,60], C_2H_2 is identified as a species of particular relevance during gas phase CH_4 pyrolysis. Specifically, at a temperature of 1673 K and a H_2:CH_4 feed ratio of 1 (Fig. 7(a)), C_2H_2 reaches a maximum of 6 mol-% at the inlet of the packed bed, before it is quickly consumed within the bed reaching a negligible amount at the reactor outlet. Our simulations suggest similar trends also for 1573 and 1673 K for all the H_2:CH_4 ratios (Fig. 7(b) and (c)), whereas at 1473 K, the C_2H_2 mole fraction continues to increase downstream of the packed bed before sharply decreasing approx. 0.25 m before the reactor outlet. Furthermore, increasing the H_2:CH_4 feed ratio decreases the peak mole fractions, which suggests a suppression of C_2H_2 formation as gaseous by-product.

Axial profiles of C_6H_6 are shown in Fig. 8(a), (b) and (c). At 1673 K, the simulations suggest a peak mole fraction even prior to the packed bed. At 1573 K, the peak appears just at the entrance of bed, whereas there is no peak at 1473 K but rather a steady increase along the reactor length. However, an increase of the H_2:CH_4 feed ratio suppresses C_6H_6 formation. Notably, even though the mole fractions of by-products are in

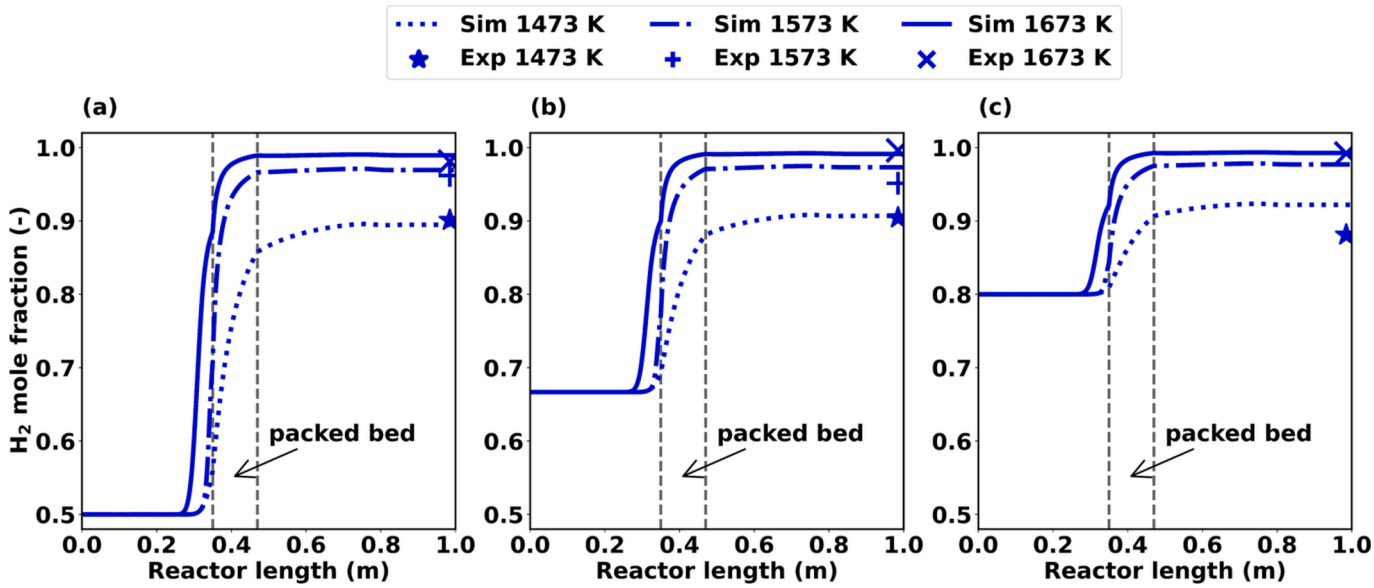

Fig. 6. Elucidation of main product H_2 along reactor length for different temperatures along with experimental comparison; (a) H_2:CH_4 molar feed ratio of 1, (b) ratio of 2, (c) ratio of 4. Lines represent simulation results while markers represent end-of-pipe experimental measurements.

very small quantities, model results agree well to the experiments underlining the accuracy.

Overall, the model accuracy remains particularly high between hot zone temperatures of 1473 K and 1873 K. For H_2:CH_4 feed ratio of 4 and 1473 K, the model tends to over predict H_2 formation while under predicting C_2H_2 and C_6H_6. It can be attributed to stronger H_2 inhibition of deposition reactions in experiments discussed in section 4.1.3. Furthermore, gaseous by-products are formed within the reactor in the pre-heating zone as well as in the packed bed, but typically decline towards negligible values by the reactor outlet that are close to the calibration limits of the analytical instruments. Note, that for such data a generous estimation of the measurement errors may sum up to ± 5 % of the absolute value, which only allows to derive some general trends for the by-product concentrations. The mole fraction trend of the most important by-product C_2H_2 at 1473 K, that strongly differs from those predicted for 1573 K and 1673 K (Fig. 7) can be explained by a trade-off between C_2H_2 formation in the gas-phase and C_2H_2 consumption in the carbon particle packed bed due to carbon deposition reactions. Although C_2H_2 is still formed in the gas-phase downstream of the packed bed since CH_4 conversion still takes place, only the reactor walls remain available for deposition; therefore, the deposition reaction rate is smaller than in the packed bed with its substantially higher surface area. As a consequence, the trade-off results in net C_2H_2 production (reactor length 0.5 m to 0.75 m). Antes et al. [94] reported a similar effect on the deposition reaction by varying the area/volume ratio of the packing material. The further drop in the molar fraction of C_2H_2 that is observed from a reactor position of 0.75 m onwards occurs due to reverse reactions in the gas-phase [72]. Analogous to C_2H_2, also C_2H_4 forms prior to the packed bed. Since according to the gas-phase reaction sequence C_2H_4 forms prior to C_2H_2 (Fig. 3), the peak concentration of C_2H_4 is observed earlier along the reactor axis, as illustrated in Fig. S2(a), (b) and (c). The peak concentration of C_6H_6 just in front of the packed bed can be explained by the trade-off between slow C_6H_6 formation in the gas-phase and a quick consumption due to deposition. At 1473 K, C_6H_6 deposition is slower than higher temperatures. This leads to a steady increase in C_6H_6 along the reactor axis at 1473 K. Furthermore, increasing the H_2:CH_4 ratio

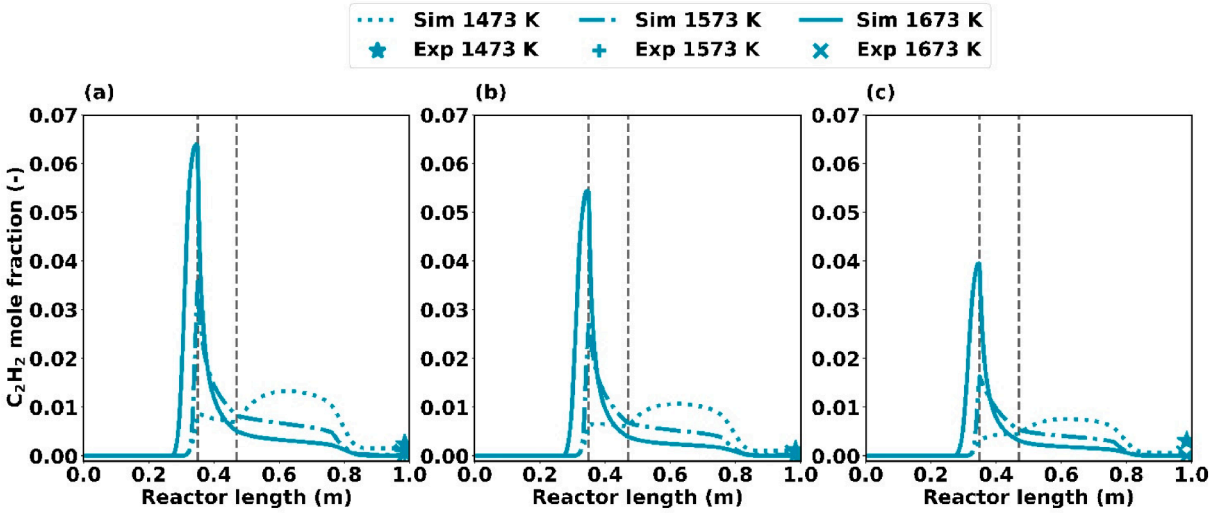

Fig. 7. Axial profiles of main gas phase by-product C_2H_2 along with experimental comparison; (a) H_2:CH_4 molar feed ratio of 1, (b) ratio of 2, (c) ratio of 4. Lines represent simulation results while points represent end-of-pipe experimental measurements.

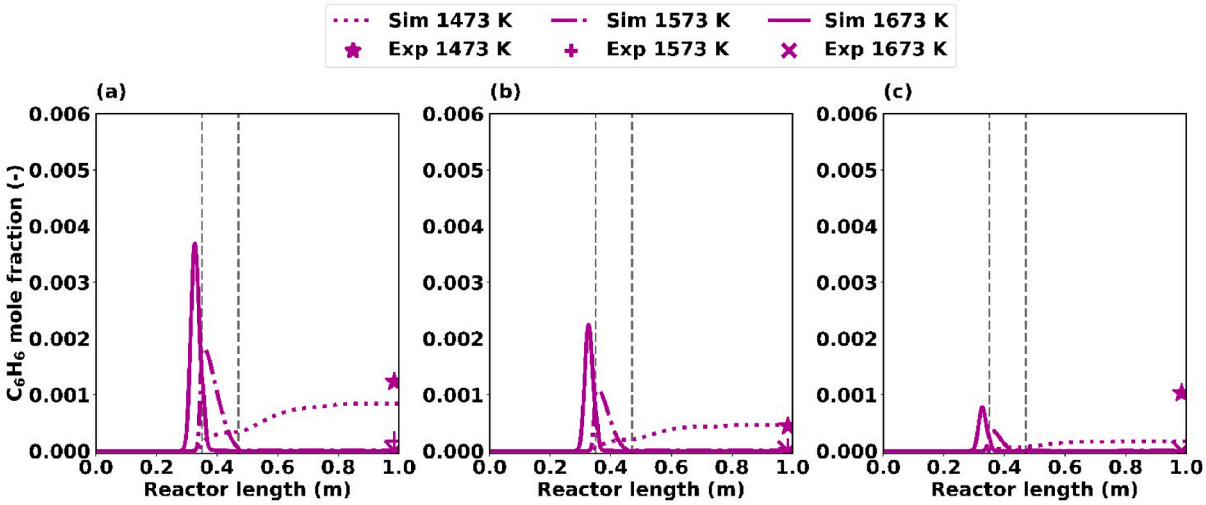

Fig. 8. Axial profiles of C_6H_6 along with experimental comparison; (a) H_2:CH_4 molar feed ratio of 1, (b) ratio of 2, (c) ratio of 4. Lines represent simulation results while points represent end-of-pipe experimental measurements.

suppresses peak mole fraction of C_6H_6 (Fig. 8) and also of C_2H_2 (Fig. 7). This can be attributed to hydrogen inhibition phenomena. Therefore, temperature and H_2:CH_4 feed ratio are the critical process parameters to achieve high CH_4 conversion and to simultaneously control by-product formation. Furthermore, the availability of surface area and the fact that reverse reactions can take place also influence gas-phase species.

4.1.2. Soot formation

The exploration of temperature and H_2:CH_4 feed ratio effects on the primary formation of soot is presented here, pivoting focus on simulation results due to the typically low quantity of soot observed during the experimental measurement campaign.

Fig. 9 demonstrates the influence of H_2:CH_4 ratio and temperature on the particle number concentration and clearly shows that soot formation ahead of the bed across all temperatures and feed molar ratios takes place. Rising temperatures lead to an earlier and accelerated soot formation primarily due to the formation of pyrene dimers, which are favored at higher temperatures (Fig. 9(a)). A peak in the soot particle concentration emerges when the pyrene dimer formation rate aligns with the coagulation rate, and this peak becomes more prominent with increasing temperature. Inside the bed, the particle number concentration decreases sharply at elevated temperatures and H_2:CH_4 ratios, attributed to the increased coagulation rate due to the limited space for soot particles, resulting in more collisions (Fig. 9(b)). Moving to the post-hot zone downstream the packed bed, the collision rate decreases, causing a slower reduction in soot particle concentration. Towards the end of the bed, the soot particle number concentration becomes relatively stable, primarily due to the formation of more pyrene dimers via reversible reactions in the gas-phase at lower temperatures, thereby escalating soot nucleation rates (Fig. 9(c)). This effect is particularly significant at 1473 K, leading to a surge in particle numbers, a gradual decrease, and ultimately a consistent soot particle number towards the bed's end. On the other hand, the H_2:CH_4 ratio exerts minimal influence on the soot particle number concentration within the reactor at 1573 K and 1673 K (Fig. 9). At 1473 K, however, gas-phase chemistry takes the forefront, significantly driving soot formation. At this temperature, an increased H_2:CH_4 ratio results in a slower growth of the particle number concentration in the bed due to the gradual formation of the pyrene dimer that competes with the coagulation rate. In the post-hot zone, the particle number concentration diminishes as the H_2:CH_4 ratio increases due to reversible gas-phase reactions. This shift is also marked by a rightward movement of the peak of soot particle number, indicating a slower soot nucleation process (Fig. 9(c)).

Moreover, Fig. 10 offers insights into the influence of H_2:CH_4 ratio

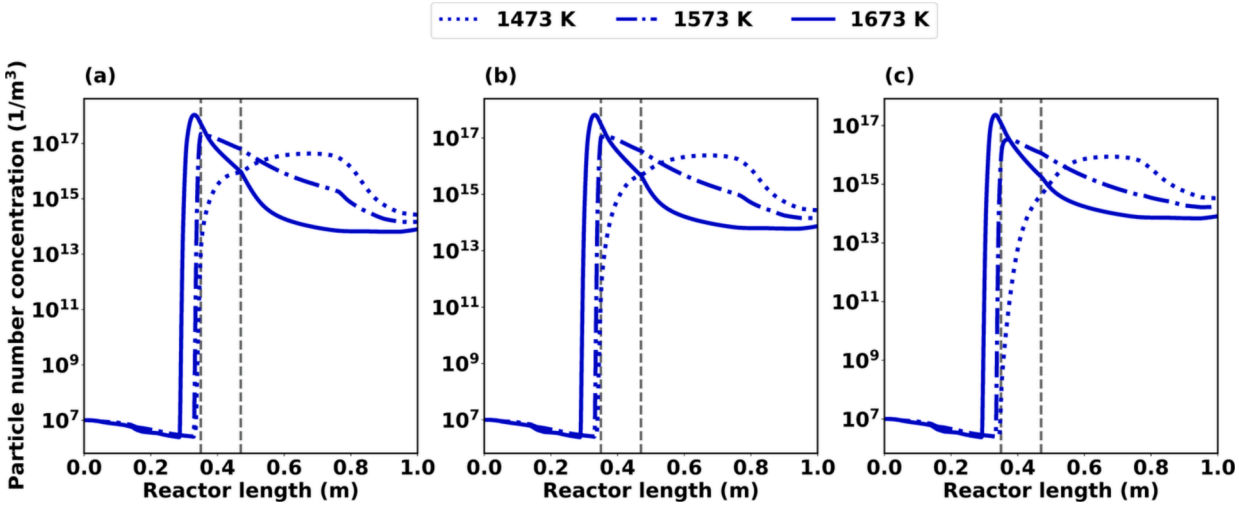

Fig. 9. Simulated particle number concentration along the reactor length; (a) H_2:CH_4 molar feed ratio of 1, (b) ratio of 2, and (c) ratio of 4.

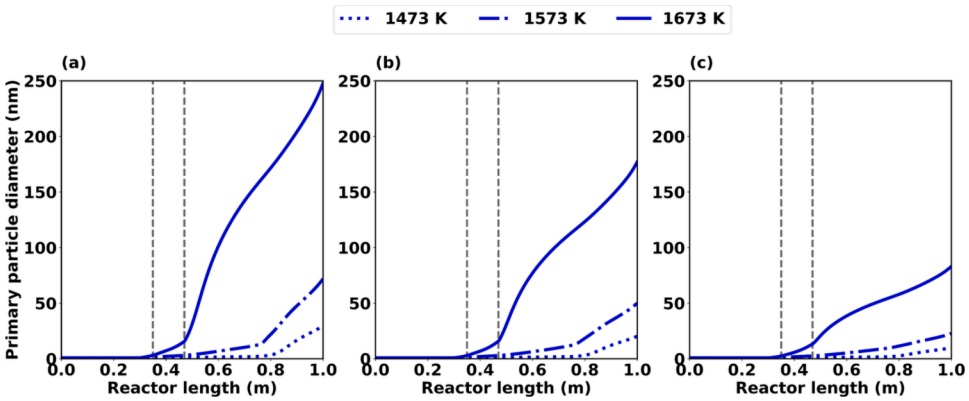

Fig. 10. Simulated primary particle diameter along the reactor length; (a) H_2:CH_4 molar feed ratio of 1, (b) ratio of 2, and (c) ratio of 4.

and temperature on the soot primary particle diameter along the reactor axis. According to the simulation data in Fig. 10(a), the highest primary particle diameter of 248 nm is found at an H_2:CH_4 ratio of 2 at 1673 K, whereas the smallest particle diameter of 21 nm is predicted at an H_2:CH_4 ratio of 4 at 1473 K (Fig. 10(c)). The axial profiles of the soot primary particle diameter reveal a gradual initial growth, followed by a more dramatic surge towards the reactor outlet. This sharp increase in primary particle diameter can be explained by an increase in collision rate at higher temperatures. The slow yet continuous rise of the nucleation rate, which diminishes the collision effect with an increasing H_2:CH_4 ratio, contributes to a reduction of the primary soot particle diameter.

In summary, the exploration of the interplay between temperatures, H_2:CH_4 ratio, and their effects on soot formation provides several information. In particular, an increasing temperature results in a decrease of the soot particle number concentration and a corresponding increase of the soot particle diameter. Conversely, an increasing H_2:CH_4 ratio correlates with a rising particle number concentration and a decreasing primary particle diameter. These trends provide a deeper understanding of the mechanisms involved in soot formation, emphasizing the key roles temperature and H_2:CH_4 ratio play in influencing the particle number concentration and primary particle diameter.

4.1.3. Deposition

Similar to soot formation, the quantification of carbon depositions is only possible after finishing an experiment and in addition, the experimental setup design does not allow to gain data with spatial resolution. Therefore, the present section focuses on the quantitative analysis of deposited carbon by means of simulations. Fig. 11 shows the impact of temperature and H_2:CH_4 feed ratio on axial carbon deposition profiles along the reactor length. Deposition begins on the reactor wall already before the reaction gases reach the carbon particles packed bed and raises rapidly upon entering the bed. Herein, the temperature exerts a significant influence on both the deposition profile and the quantity of deposition. At 1673 K and 1573 K most of the deposition takes place at the beginning of the bed, regardless of the H_2:CH_4 feed ratio (Fig. 11(a), (b), (c)), whereas at 1473 K a more uniform deposition across the packed bed is achieved. A total of 0.91 g carbon deposition is estimated by simulations at 1473 K and a H_2:CH_4 feed ratio of 2, which increases to 1.21 g at 1573 K and to 1.23 g at 1673 K. Although the amount of CH_4 in the feed is lower by default with an increase of the H_2:CH_4 feed ratio from 2 to 4 at 1473 K, decreases the carbon deposition by around 10 % (in relation to the respective amount of CH_4 in the feed). It is therefore important to simultaneously compare the effect of the H_2:CH_4 feed ratio on both CH_4 conversion and the carbon deposition amount. At 1673 and 1573 K, CH_4 conversion is only slightly reduced if the H_2 content in the feed increases, therefore the deposition reduction is related to the lower carbon level in the feed. On the other hand, increasing the H_2:CH_4 feed ratio from 1 to 4 at 1473 K reduces CH_4 conversion from 74 % to 59 %, which goes along with a reduction of the deposited carbon amount from 1.48 g to 0.46 g.

Since there are two surface mechanisms considered in the current study, i.e. soot formation and carbon deposition, it is important to compare solid carbon formation estimates from different mechanisms. For a temperature of 1673 K and a H_2:CH_4 feed ratio of 2, solid carbon formed due to soot is 6.6 mg compared to 1.23 g due to surface

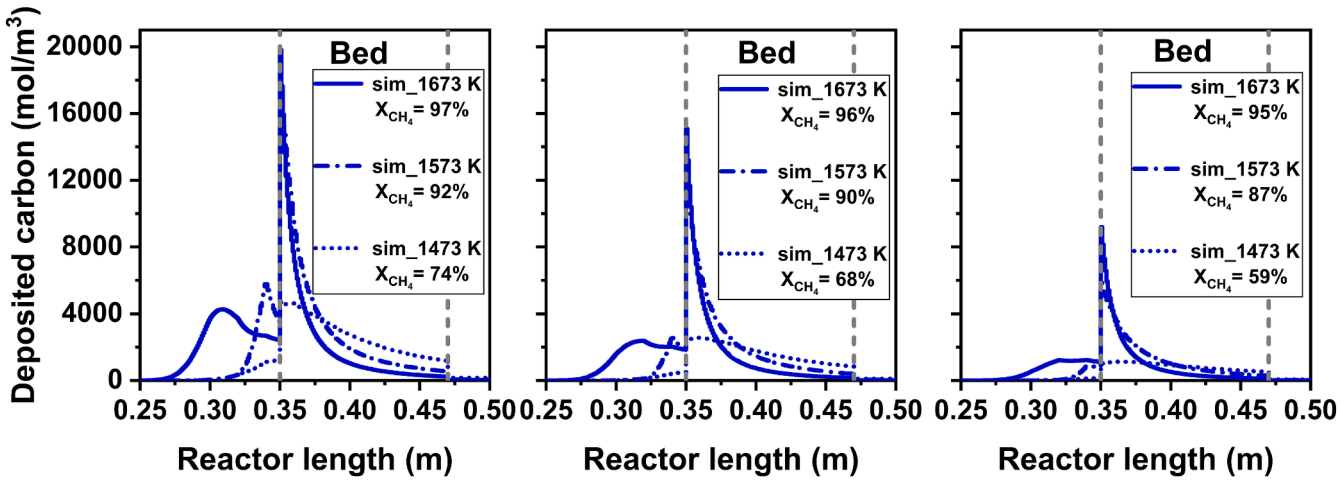

Fig. 11. Deposition profiles along the reactor length for $\tau = 5$ s, $p = 1$ bar; (a) H_2:CH_4 molar feed ratio of 1, (b) ratio of 2, and (c) ratio of 4.

deposition. Carbon formed due to soot remains below 20 mg for the process conditions considered in this study.

Overall, deposition is the dominant mechanism resulting in solid carbon formation compared to soot formation. This can be explained by the large surface area that is available for deposition, whereas only limited space and residence time are available for gas-phase reactions resulting in PAHs and then soot particles formation. Since gas-phase deposition precursors (C_2H_2, C_6H_6, C_2H_4, and C_2H_6) are also formed in the pre-heating zone, deposition starts already on the pre-heating zone wall (Fig. 11). However, the rapid increase in the deposition at the entrance of the bed can be attributed to a much larger surface area in the packed bed compared to the empty tube reactor walls.

Furthermore, the temperature exerts a profound influence on both, the deposition profile and the deposition quantity. At 1473 K deposition occurs uniformly throughout the bed. This uniform deposition distribution is desirable, as excessive deposition at the beginning of the reactor bed can lead to reactor clogging. Nevertheless, it comes at the cost of substantially lower CH_4 conversion at 1473 K compared to the higher temperatures. The H_2:CH_4 feed ratio is a vital reaction control parameter for temperatures below 1573 K. At 1473 K CH_4 conversion is reduced by 15 % when H_2:CH_4 feed ratio is increased from 1 to 4, which can be attributed to H_2 inhibition that is less pronounced for higher temperatures [70].

4.2. Impact of residence time

The impact of residence time (τ) in the hot zone on the CH_4 pyrolysis process is studied in this section. Simulations are performed to analyze the behavior of gas-phase species, soot formation, and deposition.

4.2.1. Gas-phase species

Fig. 12 illustrates the influence of τ on H_2 production at 1473, 1573 and 1673 K. The impact of τ on H_2 formation is particularly pronounced at 1473 K, where increasing τ from 1 s to 3 s results in a significant rise in H_2 production (Fig. 12 (a)). In contrast, the subsequent increase in H_2 formation is relatively small when τ is increased from 5 s to 7 s. This trend persists as the temperature rises to 1573 K and 1673 K, as shown in Fig. 12(b) and (c), respectively.

Axial profiles of the main gas-phase by-product C_2H_2 are shown in Fig. 13. At 1473 K, a peak of C_2H_2 is obtained at the entrance of the bed for τ of 5 s and 7 s, whereas for 1 s and 3 s a steady increase is observed (Fig. 13(a)). At a temperature of 1573 K, the axial profiles of H_2 formation exhibit distinct characteristics. In the case of 1 s residence time, an increase in H_2 formation is observed along the length of the bed. However, for residence times of 3 s, 5 s, and 7 s, the profiles display peaks at the beginning of the bed, as illustrated in Fig. 13(b). A further increase in temperature to 1673 K leads to nearly similar C_2H_2 profiles for all residence times (Fig. 13(c)). Notably, considerably higher C_2H_2 levels form at a residence time of 1 s compared to 7 s. This trend remains true for all the temperatures presented.

Overall, residence time has significant impact on the CH_4 pyrolysis product distribution. The impact of τ on H_2 production is particularly pronounced at a temperature of 1473 K, where H_2 production decreases sharply when τ is below 3 s. As τ decreases, C_2H_2 share in the by-products increases, and the highest C_2H_2 formation occurs at τ of 1 s. When τ is shorter, gas-phase C-C coupling reactions are limited in their progression, leading to the formation of only light hydrocarbons. Additionally, the contact time between the gas-phase and the particles in the packed bed is minimal, resulting in the escape of C_2H_2 and unreacted CH_4, as depicted in Fig. 13. It is consistent with previous studies [95,96] which have reported increased selectivity towards C_2H_2 and other C_2 hydrocarbons for residence times below 1 s.

4.2.2. Soot formation

It is consensus that the formation of soot strongly depends on the generation of PAHs in the gas-phase [35,49,57]. A longer τ provides opportunity for gas-phase reactions to advance towards the production of PAHs, consequently resulting in elevated soot formation and particle growth. These findings emphasize the crucial role of τ in shaping the intricate relationship between PAHs and soot formation. Consequently, longer residence time provides more time for the growth and accumulation of PAHs, leading to increased soot formation. Fig. 14 illustrates the influence of τ and temperature on the primary particle diamter. An increase in temperature promotes the formation of pyrene dimers, which in turn leads to a higher primary particle diameter at a residence time of 5 s (c.f. Fig. 10). While at 1473 K (Fig. 14(a)), the residence time barely influences the primary particle diameter, the effect becomes more pronounced with increasing temperature, as depicted in Fig. 14(b) for 1573 K and intensifies even further at 1673 K, as shown in Fig. 14(c). At 1673 K and a τ of 1 s, the primary particle diameter remains below 50 nm; it more than doubles at 3 s and finally primary particle diameters of 177 nm and 205 nm are obtained at 5 s and 7 s, respectively. It is noteworthy that the growth of primary particle diameter slows down after a residence time of 5 s. These findings underscore the intricate interplay between residence time, temperature, and primary particle diameter, providing valuable insights into the behavior of the reaction system.

4.2.3. Deposition

This section analyzes the impact of τ and temperature on the deposition. As depicted in Fig. 15(a), the deposition remains relatively uniform throughout the bed at 1473 K, especially for $\tau = 1$ s. The corresponding CH_4 conversion is only 42 %, but increases to 72 % when increasing τ to 7 s. At 1573 K, an increase of τ from 1 s to 7 s increases CH_4 conversion from 81 % to 91 %, which points to a reduced influence of residence time compared to 1473 K. Furthermore, the deposition profiles change with temperature: deposition becomes more pronounced at the bed entrance as the temperature is increased.

Moreover, the model predicts a reduction in bed-voidage with time

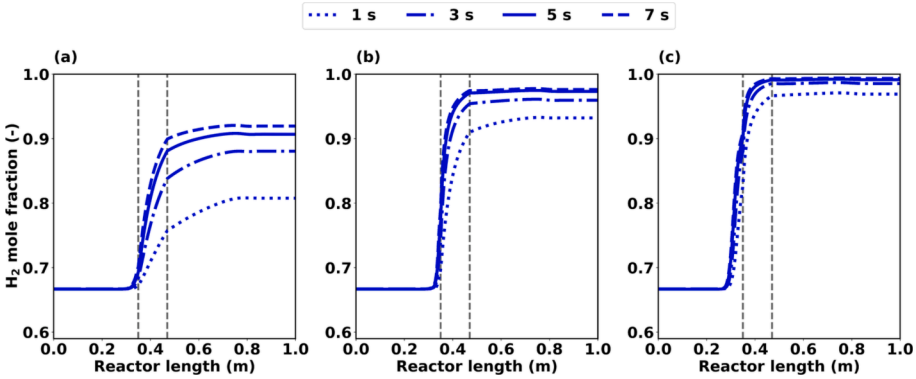

Fig. 12. H_2 production along the reactor length for different residence times keeping H_2:CH_4 feed ratio 2 and $p = 1$ bar; (a) 1473 K, (b) 1573 K, and (c) 1673 K.

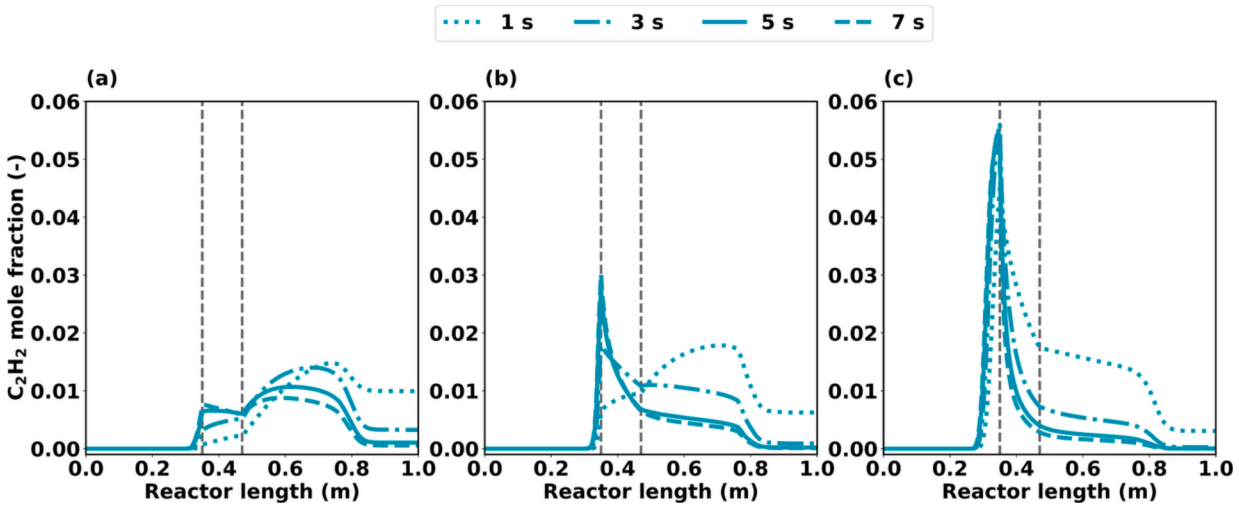

Fig. 13. C_2H_2 production along the reactor length for different residence times keeping H_2:CH_4 feed ratio 2 and $p = 1$ bar; (a) 1473 K, (b) 1573 K, and (c) 1673 K.

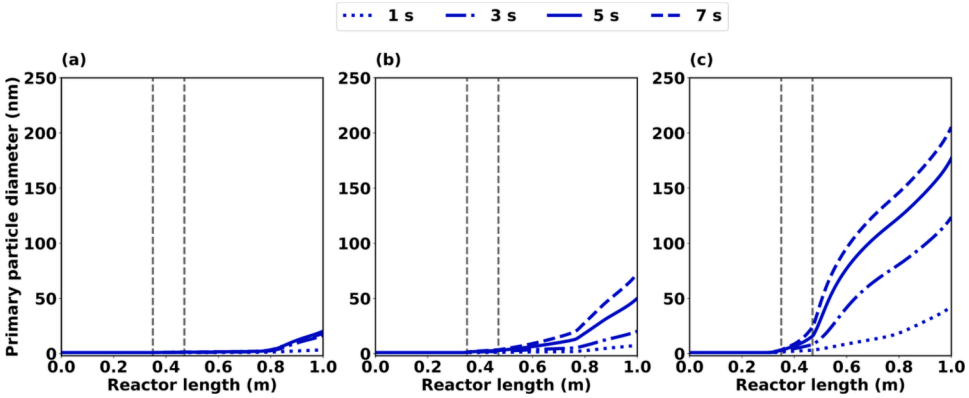

Fig. 14. Primary particle diameter as a function of the reactor length for different residence times, while keeping a H_2:CH_4 feed ratio 2 and a $p = 1$ bar; (a) 1473 K, (b) 1573 K, and (c) 1673 K.

due to carbon and soot deposition. Fig. 16 shows the evolution of bed-voidage after 10, 30, and 60 min of reactor operation at τ of 1 s (Fig. 16(a)) and 5 s (Fig. 16(b)). The most pronounced bed-voidage changes occur at the entrance of the bed where the deposition is maximal. In the case of a 1 s residence time, the bed-voidage decreases from 0.38 at the beginning of the operation to 0.11 after 20 min of operation. Conversely, with a 5 s residence time, even after 60 min of operation, the bed-voidage only drops to 0.23 from the initial value of 0.38. Since a lower residence time is concomitant with an increasing mass flow rate, more CH_4 enters the reactor at a τ of 1 s compared to 5 s. Depending on the operating conditions and CH_4 conversion, more carbon deposits at a τ of 1 s compared to higher residence times, as underscored by the data shown in Fig. 15.

Overall, the residence time has a significant influence on the deposition of carbon. The increasing carbon deposition at low residence times results in very high changes in bed-voidage with operating time, e.g. as illustrated in Fig. 16(a) for $\tau = 1$ s, that can ultimately cause clogging of the reactor. Therefore, it is crucial to obtain reliable simulation data that predict the operation time before the reactor has to be stopped due to clogging.

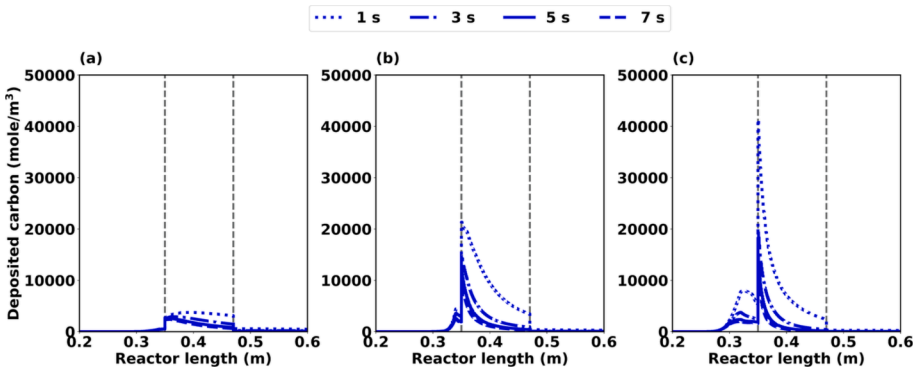

Fig. 15. Deposited carbon profiles along the reactor length for a H_2:CH_4 feed ratio 2, $p = 1$ bar, and $\tau = 1$, 3, 5, and 7 s (a) 1473 K, (b) 1573 K and (c) 1673 K.

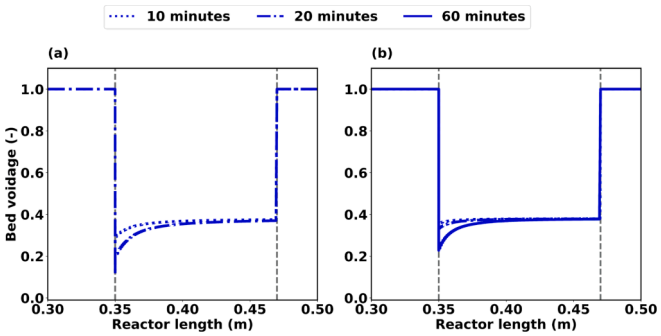

Fig. 16. Evolution of packed bed-voidage with operation time at 1673 K, H_2:CH_4 feed ratio 0 and $p = 1$ bar (a) $\tau = 1$ s, (b) $\tau = 5$ s.

The simulations conducted in this study using a comprehensive reactor model show good agreement with the end-of-pipe gas-phase measurements, highlighting its reliability and robustness. The RMSE analysis demonstrates good agreement between experiments and simulations. Additionally, the model presented is highly efficient in terms of computation; it can be executed on a single core in just a few minutes, thereby enabling rapid analysis of both the chemical kinetics and the system as a whole. This combination of high accuracy and swift processing significantly enhances the model's utility in practical applications and make it particularly attractive for upscaling. The evaluated model can be utilized to obtain axially resolved data of gas-phase species, both major and minor, as well as carbon deposition. This allows for the assessment and optimization of H_2 yield and CH_4 conversion while minimizing by-products formation. Avoiding the formatting of by-products is crucial because their presence in the effluent product gas stream would necessitate additional downstream separation processes. Furthermore, the model's capability to provide axially resolved profiles for deposited carbon and bed-voidage enables the implementation of preventive measures to avoid clogging in the reactor. However, further enhancements are required to improve the model's accuracy specifically within the low temperature from 1273 to 1473 K and high H_2:CH_4 feed ratio. To achieve this, it is crucial to move beyond the global kinetic approach employed in this work and incorporate a microkinetic description of heterogeneous deposition reactions [97,98]. Such advancements in model development can contribute significantly to the field, paving the way for more efficient and optimized CH_4 pyrolysis processes in industrial applications.

5. Conclusions

A packed bed reactor model was expanded to incorporate soot formation via the method of moment model. Furthermore, a detailed gas-phase mechanism describing the pyrolysis of CH_4 was coupled with a newly developed deposition mechanism.

Numerical simulations, which integrate both homogeneous and heterogeneous chemistry, shows a good agreement with packed bed reactor experiments at temperatures exceeding 1473 K. Key process parameters of CH_4 pyrolysis, namely temperature, H_2:CH_4 ratio, and residence time, are highlighted. Notably, temperatures above 1673 K result in over 94 % CH_4 conversion and nearly 100 % H_2 yield. With rising temperature, the model predicts an increasing primary particle diameter of soot, but a decreasing particle number concentration. Furthermore, the residence time plays a crucial role, particularly at higher residence time, which favors the formation of pyrene dimers in the gas phase and consequently results in an increasing soot particle size. Among the carbon deposition and soot formation processes investigated, deposition was found to be the dominant phenomenon. Temperature notably affects axial deposition profiles; at 1473 K, deposition is uniformly distributed across the bed, whereas at elevated temperatures, such as 1573 K and 1673 K, significant deposition primarily occurs at the bed entrance. Additionally, shorter residence times, correlated with higher inlet mass flow rates, lead to increased deposition at the bed entrance, potentially reducing bed-voidage significantly and leading to reactor clogging. The H_2:CH_4 molar feed ratio's influence on CH_4 conversion become particularly evident at temperatures below 1573 K. Above this temperature, the effect of temperature supersedes the inhibition effect of hydrogen. Therefore, controlling the H_2 content in the feed, along with temperature and residence time, can be utilized to regulate the reaction and mitigate carbon deposition.

In conclusion, the simulations presented herein that rely on a novel model integrating gas-phase, soot formation, and carbon deposition, offer a comprehensive understanding of CH_4 pyrolysis. The model does not only provide insights that are of academic relevance, but it is also valuable resource for reactor scale-up and process development in this field. Beyond predicting simple end-of-pipe, the model also provides spatially resolved information on deposition and bed-voidage, which are challenging to obtain experimentally. Notably, computational costs are low and the simulations can be run on a desktop computer within reasonable time frames. Moreover, the model presented herein, for the first time, serves as a universal tool to describe a variety of processes, including flame pyrolysis, diesel particulate filters, coke formation, and chemical vapor deposition, whenever deposition is relevant.

CRediT authorship contribution statement

Manas Mokashi: Writing – original draft, Visualization, Validation, Methodology, Investigation, Formal analysis, Data curation, Conceptualization. **Akash Bhimrao Shirsath:** Writing – original draft, Visualization, Validation, Methodology, Investigation, Formal analysis, Data curation, Conceptualization. **Ahmet Çelik:** Investigation, Formal analysis. **Patrick Lott:** Writing – review & editing, Supervision, Project administration, Methodology, Data curation. **Heinz Müller:** Investigation, Formal analysis. **Steffen Tischer:** Writing – review & editing, Supervision, Software, Formal analysis. **Lubow Maier:** Writing – review & editing, Supervision, Project administration, Formal analysis, Conceptualization. **Johannes Bode:** Writing – review & editing, Project administration, Formal analysis, Conceptualization. **David Schlereth:** Project administration, Formal analysis, Conceptualization. **Frederik Scheiff:** Project administration, Formal analysis, Conceptualization. **Dieter Flick:** Project administration, Formal analysis, Conceptualization. **Michael Bender:** Project administration, Formal analysis, Conceptualization. **Kai Ehrhardt:** Writing – review & editing, Project administration, Formal analysis, Conceptualization. **Olaf Deutschmann:** Writing – review & editing, Supervision, Resources, Project administration, Funding acquisition, Data curation, Conceptualization.

Declaration of competing interest

The authors declare that they have no known competing financial interests or personal relationships that could have appeared to influence the work reported in this paper.

Acknowledgments

We thank R. Pashminehazar, T. Sheppard, and J.-D. Grunwaldt (all KIT) for fruitful discussions and experimental support. The Federal Ministry of Education and Research (BMBF) of Germany is acknowledged for funding of the project Me^2H_2, grant number 03SF0571A-G, and omegadot software & consulting GmbH is acknowledged for a cost-free academic license of DETCHEM™.

Appendix A. Supplementary data

Supplementary data to this article can be found online at https://doi.org/10.1016/j.cej.2024.149684.

References

[1] G.A. Olah, A. Goeppert, G.K.S. Prakash. Beyond Oil and Gas: The Methanol Economy, Second Edition, Wiley-VCH, Weinheim, 2009, https://doi.org/10.1002/9783527627806.

[2] P. Lott, O. Deutschmann, Heterogeneous chemical reactions—A cornerstone in emission reduction of local pollutants and greenhouse gases, Proc. Combust. Inst. 39 (2023) 3183–3215, https://doi.org/10.1016/j.proci.2022.06.001.

[3] K. Oshiro, S. Fujimori, Role of hydrogen-based energy carriers as an alternative option to reduce residual emissions associated with mid-century decarbonization goals, Appl. Energy 313 (2022) 118803, https://doi.org/10.1016/j.apenergy.2022.118803.

[4] N. Sánchez-Bastardo, R. Schlögl, H. Ruland, Methane Pyrolysis for CO_2-Free H_2 Production: A Green Process to Overcome Renewable Energies Unsteadiness, Chem. Ing. Tech. 92 (2020) 1596–1609, https://doi.org/10.1002/cite.202000029.

[5] O. Machhammer, A. Bode, W. Hormuth, Financial and Ecological Evaluation of Hydrogen Production Processes on Large Scale, Chem. Eng. Technol. 39 (2016) 1185–1193, https://doi.org/10.1002/ceat.201600023.

[6] J.M. Bergthorson, Recyclable metal fuels for clean and compact zero-carbon power, Prog. Energy Combust. Sci. 68 (2018) 169–196, https://doi.org/10.1016/j.pecs.2018.05.001.

[7] C. Kuhn, A. Düll, P. Rohlfs, S. Tischer, M. Börnhorst, O. Deutschmann, Iron as recyclable energy carrier: Feasibility study and kinetic analysis of iron oxide reduction, Appl. Energy Combust. Sci. 12 (2022) 100096, https://doi.org/10.1016/j.jaecs.2022.100096.

[8] A. Düll, P. Rohlfs, O. Deutschmann, M. Börnhorst, Performance Evaluation of KBH_4 as Energy Carrier for Shipping Applications, Chem. Ing. Tech. 94 (2022) 747–759, https://doi.org/10.1002/cite.202100193.

[9] O. Schmidt, A. Gambhir, I. Staffell, A. Hawkes, J. Nelson, S. Few, Future cost and performance of water electrolysis: An expert elicitation study, Int. J. Hydrogen Energy 42 (2017) 30470–30492, https://doi.org/10.1016/j.ijhydene.2017.10.045.

[10] J. Horlyck, C. Lawrey, E.C. Lovell, R. Amal, J. Scott, Elucidating the impact of Ni and Co loading on the selectivity of bimetallic NiCo catalysts for dry reforming of methane, Chem. Eng. J. 352 (2018) 572–580, https://doi.org/10.1016/j.cej.2018.07.009.

[11] A. Giehr, L. Maier, S. Angeli, S.A. Schunk, O. Deutschmann, Dry and Steam Reforming of CH_4 on Co-hexaaluminate: On the Formation of Metallic Co and Its Influence on Catalyst Activity, Ind. Eng. Chem. Res. 59 (2020) 18790–18797, https://doi.org/10.1021/acs.iecr.0c03522.

[12] S. Hanf, S. Angeli, D. Dussol, C. Fritsch, L. Maier, M. Müller, O. Deutschmann, S. A. Schunk, Methane Dry Reforming, in: G. Stefanidis, A. Stankiewicz (Eds.), Chemical Valorisation of Carbon Dioxide, The Royal Society of Chemistry, 2022, pp. 187–207, https://doi.org/10.1039/9781839167645-00187.

[13] M.H. Halabi, M.H.J.M. de Croon, J. van der Schaaf, P.D. Cobden, J.C. Schouten, Modeling and analysis of autothermal reforming of methane to hydrogen in a fixed bed reformer, Chem. Eng. J. 137 (2008) 568–578, https://doi.org/10.1016/j.cej.2007.05.019.

[14] O. Deutschmann, L.D. Schmidt, Modeling the partial oxidation of methane in a short-contact-time reactor, AIChE J. 44 (1998) 2465–2477, https://doi.org/10.1002/aic.690441114.

[15] R. Schwiedernoch, S. Tischer, C. Correa, O. Deutschmann, Experimental and numerical study on the transient behavior of partial oxidation of methane in a catalytic monolith, Chem. Eng. Sci. 58 (2003) 633–642, https://doi.org/10.1016/S0009-2509(02)00589-4.

[16] J.P. Ciferno, J.J. Marano. Benchmarking Biomass Gasification Technologies for Fuels, Chemicals and Hydrogen Production, 2002. https://netl.doe.gov/sites/default/files/netl-file/BMassGasFinal.pdf.

[17] A.P. Simpson, A.E. Lutz, Exergy analysis of hydrogen production via steam methane reforming, Int. J. Hydrogen Energy 32 (2007) 4811–4820, https://doi.org/10.1016/j.ijhydene.2007.08.025.

[18] L. Weger, A. Abánades, T. Butler, Methane cracking as a bridge technology to the hydrogen economy, Int. J. Hydrogen Energy 42 (2017) 720–731, https://doi.org/10.1016/j.ijhydene.2016.11.029.

[19] M. Hadian, K.A. Buist, A.N.R. Bos, J.A.M. Kuipers, Single catalyst particle growth modeling in thermocatalytic decomposition of methane, Chem. Eng. J. 421 (2021) 129759, https://doi.org/10.1016/j.cej.2021.129759.

[20] I. Suelves, M.J. Lázaro, R. Moliner, B.M. Corbella, J.M. Palacios, Hydrogen production by thermo catalytic decomposition of methane on Ni-based catalysts: influence of operating conditions on catalyst deactivation and carbon characteristics, Int. J. Hydrogen Energy 30 (2005) 1555–1567, https://doi.org/10.1016/j.ijhydene.2004.10.006.

[21] N. Muradov, Catalysis of methane decomposition over elemental carbon, Catal. Commun. 2 (2001) 89–94, https://doi.org/10.1016/S1566-7367(01)00013-9.

[22] R. Moliner, I. Suelves, M.J. Lázaro, O. Moreno, Thermocatalytic decomposition of methane over activated carbons: influence of textural properties and surface chemistry, Int. J. Hydrogen Energy 30 (2005) 293–300, https://doi.org/10.1016/j.ijhydene.2004.03.035.

[23] Z. Bai, H. Chen, B. Li, W. Li, Catalytic decomposition of methane over activated carbon, J. Anal. Appl. Pyrolysis 73 (2005) 335–341, https://doi.org/10.1016/j.jaap.2005.03.004.

[24] T. Kreuger, W.P.M. van Swaaij, A.N.R. Bos, S.R.A. Kersten, Methane decomposition kinetics on unfunctionalized alumina surfaces, Chem. Eng. J. 427 (2022) 130412, https://doi.org/10.1016/j.cej.2021.130412.

[25] N. Muradov, F. Smith, A. T-Raissi, Catalytic activity of carbons for methane decomposition reaction, Catal. Today 102–103 (2005) 225–233, https://doi.org/10.1016/j.cattod.2005.02.018.

[26] T. Geißler, A. Abánades, A. Heinzel, K. Mehravaran, G. Müller, R.K. Rathnam, C. Rubbia, D. Salmieri, L. Stoppel, S. Stückrad, A. Weisenburger, H. Wenninger, T. Wetzel, Hydrogen production via methane pyrolysis in a liquid metal bubble column reactor with a packed bed, Chem. Eng. J. 299 (2016) 192–200, https://doi.org/10.1016/j.cej.2016.04.066.

[27] M. Gautier, V. Rohani, L. Fulcheri, Direct decarbonization of methane by thermal plasma for the production of hydrogen and high value-added carbon black, Int. J. Hydrogen Energy 42 (2017) 28140–28156, https://doi.org/10.1016/j.ijhydene.2017.09.021.

[28] A. Magazova, S. Böddeker, N. Bibinov, D.W. Agar, Systematic simulation strategy of plasma methane pyrolysis for CO_2-free H_2, Chem. Ing. Tech. 94 (2022) 690–700, https://doi.org/10.1002/cite.202100181.

[29] S. Kreuznacht, M. Purcel, S. Böddeker, P. Awakowicz, W. Xia, M. Muhler, M. Böke, A. von Keudell, Comparison of the performance of a microwave plasma torch and a gliding arc plasma for hydrogen production via methane pyrolysis, Plasma Process. Polym. 20 (2023), https://doi.org/10.1002/ppap.202200132.

[30] P. Lott, M.B. Mokashi, H. Müller, D.J. Heitlinger, S. Lichtenberg, A.B. Shirsath, C. Janzer, S. Tischer, L. Maier, O. Deutschmann, Hydrogen production and carbon capture by gas-phase methane pyrolysis: A feasibility study, ChemSusChem 16 (2023) e202300301.

[31] A. Holmen, O. Olsvik, O.A. Rokstad, Pyrolysis of natural gas: chemistry and process concepts, Fuel Process. Technol. 42 (1995) 249–267, https://doi.org/10.1016/0378-3820(94)00109-7.

[32] BASF SE, New technologies, Methane Pyrolysis (2022). https://www.basf.com/global/en/who-we-are/sustainability/we-produce-safely-and-efficiently/energy-and-climate-protection/carbon-management/innovations-for-a-climate-friendly-chemical-production.html#text-1002215085.

[33] A. Li, K. Norinaga, W. Zhang, O. Deutschmann, Modeling and simulation of materials synthesis: Chemical vapor deposition and infiltration of pyrolytic carbon, Compos. Sci. Technol. 68 (2008) 1097–1104, https://doi.org/10.1016/j.compscitech.2007.07.007.

[34] E.K. Lee, S.Y. Lee, G.Y. Han, B.K. Lee, T.J. Lee, J.H. Jun, K.J. Yoon, Catalytic decomposition of methane over carbon blacks for CO_2-free hydrogen production, Carbon 42 (2004) 2641–2648, https://doi.org/10.1016/j.carbon.2004.06.003.

[35] J. Appel, H. Bockhorn, M. Frenklach, Kinetic modeling of soot formation with detailed chemistry and physics: laminar premixed flames of C_2 hydrocarbons, Combust. Flame 121 (2000) 122–136, https://doi.org/10.1016/S0010-2180(99)00135-2.

[36] M. Frenklach, H. Wang, Detailed modeling of soot particle nucleation and growth, Symp. (Int.) Combust. 23 (1991) 1559–1566, https://doi.org/10.1016/S0082-0784(06)80426-1.

[37] M. Frenklach, Reaction mechanism of soot formation in flames, Phys. Chem. Chem. Phys. 4 (2002) 2028–2037, https://doi.org/10.1039/b110045a.

[38] J.H. Miller, Aromatic excimers: evidence for polynuclear aromatic hydrocarbon condensation in flames, Proc. Combust. Inst. 30 (2005) 1381–1388, https://doi.org/10.1016/j.proci.2004.08.192.

[39] M. Wartel, J.F. Pauwels, P. Desgroux, X. Mercier, Pyrene measurements in sooting low pressure methane flames by jet-cooled laser-induced fluorescence, J. Phys. Chem. A 115 (2011) 14153–14162, https://doi.org/10.1021/jp206970t.

[40] A.B. Shirsath, M. Mokashi, P. Lott, H. Müller, R. Pashminehazar, T. Sheppard, S. Tischer, L. Maier, J.-D. Grunwaldt, O. Deutschmann, Soot Formation in Methane Pyrolysis Reactor: Modeling Soot Growth and Particle Characterization, J. Phys. Chem. A 127 (2023) 2136–2147, https://doi.org/10.1021/acs.jpca.2c06878.

[41] W. Benzinger, A. Becker, K.J. Hüttinger, Chemistry and kinetics of chemical vapour deposition of pyrocarbon: I. Fundamentals of kinetics and chemical reaction engineering, Carbon 34 (1996) 957–966, https://doi.org/10.1016/0008-6223(96)00010-3.

[42] A. Becker, K.J. Hüttinger, Chemistry and kinetics of chemical vapor deposition of pyrocarbon—II pyrocarbon deposition from ethylene, acetylene and 1,3-butadiene in the low temperature regime, Carbon 36 (1998) 177–199, https://doi.org/10.1016/S0008-6223(97)00175-9.

[43] A. Becker, K.J. Hüttinger, Chemistry and kinetics of chemical vapor deposition of pyrocarbon - III pyrocarbon deposition from propylene and benzene in the low temperature regime, Carbon 36 (1998) 201–211, https://doi.org/10.1016/S0008-6223(97)00176-0.

[44] A. Becker, K.J. Hüttinger, Chemistry and kinetics of chemical vapor deposition of pyrocarbon - IV pyrocarbon deposition from methane in the low temperature regime, Carbon 36 (1998) 213–224, https://doi.org/10.1016/S0008-6223(97)00177-2.

[45] A. Becker, K.J. Hüttinger, Chemistry and kinetics of chemical vapor deposition of pyrocarbon - V influence of reactor volume/deposition surface area ratio, Carbon 36 (1998) 225–232, https://doi.org/10.1016/S0008-6223(97)00178-4.

[46] K.J. Hüttinger, CVD in Hot Wall reactors - the interaction between homogeneous gas-phase and heterogeneous surface reactions, Chem. Vap. Deposition 4 (1998) 151–158, https://doi.org/10.1002/(sici)1521-3862(199807)04:04<151::aid-cvde151>3.0.co;2-2.

[47] A. Li, O. Deutschmann, Transient modeling of chemical vapor infiltration of methane using multi-step reaction and deposition models, Chem. Eng. Sci. 62 (2007) 4976–4982, https://doi.org/10.1016/j.ces.2007.01.069.

[48] P.A. Tesner, S.V. Shurupov, Some physico-chemical parameters of soot formation during pyrolysis of hydrocarbons, Combust. Sci. Technol. 105 (1995) 147–161, https://doi.org/10.1080/00102209508907744.

[49] P.A. Tesner, S.V. Shurupov, Soot formation during pyrolysis of naphthalene, anthracene and pyrene, Combust. Sci. Technol. 126 (1997) 139–151, https://doi.org/10.1080/00102209708935671.

[50] G.A. Kelesidis, M.R. Kholghy, A Monodisperse Population Balance Model for Nanoparticle Agglomeration in the Transition Regime, Materials 14 (2021) 1–13, https://doi.org/10.3390/ma14143882.

[51] S. Tsantilis, S.E. Pratsinis, Soft- and Hard-Agglomerate Aerosols Made at High Temperatures, Langmuir 20 (2004) 5933–5939, https://doi.org/10.1021/la036389w.

[52] H. Bockhom, Soot formation in combustion: mechnisms and models, Springer Ser. Chem. Phys. 59 (1994) 165–192.

[53] M. Frenklach, S.J. Harris, Aerosol dynamics modeling using the method of moments, J. Colloid Interface Sci. 118 (1987) 252–261, https://doi.org/10.1016/0021-9797(87)90454-1.

[54] E.K.Y. Yapp, D. Chen, J. Akroyd, S. Mosbach, M. Kraft, J. Camacho, H. Wang, Numerical simulation and parametric sensitivity study of particle size distributions in a burner-stabilised stagnation flame, Combust. Flame 162 (2015) 2569–2581, https://doi.org/10.1016/j.combustflame.2015.03.006.

[55] C.J. Pope, J.B. Howard, Simultaneous Particle and Molecule Modeling (SPAMM): An Approach for Combining Sectional Aerosol Equations and Elementary Gas-Phase Reactions, Aerosol Sci. Tech. 27 (1997) 73–94, https://doi.org/10.1080/02786829708965459.

[56] J.Z. Wen, M.J. Thomson, S.H. Park, S.N. Rogak, M.F. Lightstone, Study of soot growth in a plug flow reactor using a moving sectional model, Proc. Combust. Inst. 30 (2005) 1477–1484, https://doi.org/10.1016/j.proci.2004.08.178.

[57] D. Aubagnac-Karkar, A. El Bakali, P. Desgroux, Soot particles inception and PAH condensation modelling applied in a soot model utilizing a sectional method, Combust. Flame 189 (2018) 190–206, https://doi.org/10.1016/j.combustflame.2017.10.027.

[58] M. Balthasar, M. Kraft, A stochastic approach to calculate the particle size distribution function of soot particles in laminar premixed flames, Combust. Flame 133 (2003) 289–298, https://doi.org/10.1016/S0010-2180(03)00003-8.

[59] J. Appel, H. Bockhorn, M. Wulkow, A detailed numerical study of the evolution of soot particle size distributions in laminar premixed flames, Chemosphere 42 (2001) 635–645, https://doi.org/10.1016/S0045-6535(00)00237-X.

[60] A. Becker, Z. Hu, K.J. Hüttinger, Hydrogen inhibition model of carbon deposition from light hydrocarbons, Fuel 79 (2000) 1573–1580, https://doi.org/10.1016/S0016-2361(00)00030-2.

[61] S.D. Angeli, S. Gossler, S. Lichtenberg, G. Kass, A.K. Agrawal, M. Valerius, K. P. Kinzel, O. Deutschmann, Reduction of CO_2 Emission from Off-Gases of Steel Industry by Dry Reforming of Methane, Angew. Chem., Int. Ed. 60 (2021) 11852–11857, https://doi.org/10.1002/anie.202100577.

[62] C.A. Schuetz, M. Frenklach, Nucleation of soot: Molecular dynamics simulations of pyrene dimerization, Proc. Combust. Inst. 29 (2002) 2307–2314, https://doi.org/10.1016/s1540-7489(02)80281-4.

[63] M. Frenklach, H. Wang, in: Detailed Mechanism and Modeling of Soot Particle Formation, Springer Ser. Chem. Phys., Springer, Berlin Heidelberg, Berlin, Heidelberg, 1994, pp. 165–192, https://doi.org/10.1007/978-3-642-85167-4_10.

[64] Q. Zhang, H. Guo, F. Liu, G.J. Smallwood, M.J. Thomson, Modeling of soot aggregate formation and size distribution in a laminar ethylene/air coflow diffusion flame with detailed PAH chemistry and an advanced sectional aerosol dynamics model, Proc. Combust. Inst. 32 I (2009) 761–768, https://doi.org/10.1016/j.proci.2008.06.109.

[65] F. Liu, X. He, X. Ma, Q. Zhang, M.J. Thomson, H. Guo, G.J. Smallwood, S. Shuai, J. Wang, An experimental and numerical study of the effects of dimethyl ether addition to fuel on polycyclic aromatic hydrocarbon and soot formation in laminar coflow ethylene/air diffusion flames, Combust. Flame 158 (2011) 547–563, https://doi.org/10.1016/j.combustflame.2010.10.005.

[66] F. Liu, Y. Ai, W. Kong, Effect of hydrogen and helium addition to fuel on soot formation in an axisymmetric coflow laminar methane/air diffusion flame, Int. J. Hydrogen Energy 39 (2014) 3936–3946, https://doi.org/10.1016/j.ijhydene.2013.12.151.

[67] A. Naseri, M.R. Kholghy, N.A. Juan, M.J. Thomson, Simulating yield and morphology of carbonaceous nanoparticles during fuel pyrolysis in laminar flow reactors enabled by reactive inception and aromatic adsorption, Combust. Flame 237 (2022) 111721, https://doi.org/10.1016/j.combustflame.2021.111721.

[68] K.C. Le, C. Lefumeux, T. Pino, Watching soot inception via online Raman spectroscopy, Combust. Flame 236 (2022) 111817, https://doi.org/10.1016/j.combustflame.2021.111817.

[69] V. Chernov, M.J. Thomson, S.B. Dworkin, N.A. Slavinskaya, U. Riedel, Soot formation with C_1 and C_2 fuels using an improved chemical mechanism for PAH growth, Combust. Flame 161 (2014) 592–601, https://doi.org/10.1016/j.combustflame.2013.09.017.

[70] P.A. Tesner, Kinetics of Pyrolytic Carbon Formation, Chem. Phys. Carbon (1984) 65–161.

[71] H. Li, A. Li, R. Bai, K. Li, Numerical simulation of chemical vapor infiltration of propylene into C/C composites with reduced multi-step kinetic models, Carbon 43 (2005) 2937–2950, https://doi.org/10.1016/j.carbon.2005.05.046.

[72] M. Mokashi, A.B. Shirsath, P. Lott, H. Müller, S. Tischer, Understanding of gas-phase methane pyrolysis towards hydrogen and solid carbon with detailed kinetic simulations and experiments, Chem. Eng. J. 479 (2024) 147556, https://doi.org/10.1016/j.cej.2023.147556.

[73] P. Deuflhard, E. Hairer, J. Zugck, One-step and extrapolation methods for differential-algebraic systems, Numer. Math. 51 (1987) 501–516, https://doi.org/10.1007/BF01400352.

[74] A.B. Shirsath, M.L. Schulte, B. Kreitz, S. Tischer, J.-D. Grunwaldt, O. Deutschmann, Spatially-resolved investigation of CO_2 methanation over Ni/γ-Al_2O_3 and $Ni_{3.2}Fe$/γ-Al_2O_3 catalysts in a packed-bed reactor, Chem. Eng. J. 469 (2023) 143847, https://doi.org/10.1016/j.cej.2023.143847.

[75] S. Ergun, A.A. Orning, Fluid Flow through Randomly Packed Columns and Fluidized Beds, Ind. Eng. Chem. 41 (1949) 1179–1184, https://doi.org/10.1021/ie50474a011.

[76] O. Deutschmann, Modeling of the Interactions Between Catalytic Surfaces and Gas-Phase, Catal. Letters. 145 (2014) 272–289, https://doi.org/10.1007/s10562-014-1431-1.

[77] O. Deutschmann, S. Tischer, S. Kleditzsch, V. Janardhanan, C. Correa, D. Chatterjee, N. Mladenov, H.D. Minh, H. Karadeniz, M. Hettel, V. Menon, A. Banerjee, H. Gossler, A. Shirsath, E. Daymo, DETCHEM, (2022). http://www.detchem.com.

[78] S. Wan, K. Keller, P. Lott, A.B. Shirsath, S. Tischer, T. Häber, R. Suntz, O. Deutschmann, Experimental and numerical investigation of NO oxidation on Pt/Al_2O_3- and NOx storage on Pt/BaO/Al_2O_3-catalysts, catal, Sci. Technol. 12 (2022) 4456–4470, https://doi.org/10.1039/d2cy00572g.

[79] K. Herrera Delgado, L. Maier, S. Tischer, A. Zellner, H. Stotz, O. Deutschmann, Surface reaction kinetics of steam- and CO_2-reforming as well as oxidation of methane over nickel-based catalysts, Catalysts 5 (2015) 871–904, https://doi.org/10.3390/catal5020871.

[80] C. Eßmann, L. Maier, A. Li, S. Tischer, O. Deutschmann, Natural Gas Steam Reforming over Rhodium/Alumina Catalysts: Experimental and Numerical Study of the Carbon Deposition from Ethylene and Carbon Monoxide, Ind. Eng. Chem. Res. 53 (2014) 12270–12278, https://doi.org/10.1021/ie5015525.

[81] H. Zhang, G. Sharma, S. Dhawan, D. Dhanraj, Z. Li, P. Biswas, Comparison of discrete, discrete-sectional, modal and moment models for aerosol dynamics simulations, Aerosol Sci. Technol. 54 (2020) 739–760, https://doi.org/10.1080/02786826.2020.1723787.

[82] S.E. Pratsinis, Simultaneous nucleation, condensation, and coagulation in aerosol reactors, J. Colloid Interface Sci. 124 (1988) 416–427, https://doi.org/10.1016/0021-9797(88)90180-4.

[83] M. Balthasar, F. Mauss, A. Knobel, M. Kraft, Detailed modeling of soot formation in a partially stirred plug flow reactor, Combust. Flame 128 (2002) 395–409, https://doi.org/10.1016/S0010-2180(01)00344-3.

[84] M. Frenklach, Method of moments with interpolative closure, Chem. Eng. Sci. 57 (2002) 2229–2239, https://doi.org/10.1016/S0009-2509(02)00113-6.

[85] A. Kazakov, M. Frenklach, Dynamic modeling of soot particle coagulation and aggregation: implementation with the method of moments and application to high-pressure laminar premixed flames, Combust. Flame 114 (1998) 484–501, https://doi.org/10.1016/S0010-2180(97)00322-2.

[86] M.J. Thomson, Modeling soot formation in flames and reactors: Recent progress and current challenges, Proc. Combust. Inst. 39 (2023) 805–823, https://doi.org/10.1016/j.proci.2022.07.263.

[87] K.W. Lee, J.A. Gieseke, Collection of aerosol particles by packed beds, Environ. Sci. Technol. 13 (1979) 466–470, https://doi.org/10.1021/es60152a013.

[88] D.R. Cox, W. Feller, An Introduction to Probability Theory and Its Applications. (1958), https://doi.org/10.2307/2342907.

[89] B.E. Logan, D.G. Jewett, R.G. Arnold, E.J. Bouwer, C.R. O'Melia, Clarification of Clean-Bed Filtration Models, J. Environ. Eng. 121 (1995) 869–873, https://doi.org/10.1061/(asce)0733-9372(1995)121:12(869).

[90] N.A. Fuchs, R.E. Daisley, M. Fuchs, C.N. Davies, M.E. Straumanis, The Mechanics of Aerosols, Phys. Today 18 (1965) 73, https://doi.org/10.1063/1.3047354.

[91] I. Langmuir, Mathematical Investigation of Water Droplet Trajectories, Army Air Forces Headquarters, Air Technical Service Command (1961), https://doi.org/10.1016/b978-0-08-009362-8.50022-3.

[92] R. Pfeffer, Heat and mass transport in multiparticle systems, Ind. Eng. Chem. Fundam. 3 (1964) 380–383, https://doi.org/10.1021/i160012a018.

[93] A.G. Konstandopoulos, J.H. Johnson, Wall-Flow Diesel Particulate Filters - Their Pressure Drop and Collection Efficiency, SAE Technical Paper 890405 (1989), https://doi.org/10.4271/890405.

[94] J. Antes, Z. Hu, W. Zhang, K.J. Huttinger, Chemistry and kinetics of chemical vapour deposition of pyrocarbon VII. confirmation of the influence of the substrate surface area/reactor volume ratio, Carbon 37 (1999) 2031–2039, https://doi.org/10.1016/S0008-6223(99)00070-6.

[95] F.G. Billaud, F. Baronnet, C.P. Gueret, Thermal coupling of methane in a tubular flow reactor: parametric study, Ind. Eng. Chem. Res. 32 (1993) 1549–1554, https://doi.org/10.1021/ie00020a003.

[96] O. Olsvik, O.A. Rokstad, A. Holmen, Pyrolysis of methane in the presence of hydrogen, Chem. Eng. Technol. 18 (1995) 349–358, https://doi.org/10.1002/ceat.270180510.

[97] M. Frenklach, H. Wang, Detailed surface and gas-phase chemical kinetics of diamond deposition, Phys. Rev. B 43 (1991) 1520–1545, https://doi.org/10.1103/PhysRevB.43.1520.

[98] R. Lacroix, R. Fournet, I. Ziegler-Devin, P.M. Marquaire, Kinetic modeling of surface reactions involved in CVI of pyrocarbon obtained by propane pyrolysis, Carbon 48 (2010) 132–144, https://doi.org/10.1016/j.carbon.2009.08.041.